

40 The determinants of bundling of the cellulose fibers, mainly their interaction with hemicelluloses and
41 pectins, are thought to be very important as they confer additional, higher-order mechanical
42 properties^{9,10}. The cellulose fibers are secreted into the cell wall by membrane-embedded hexameric
43 Cellulose Synthase Complexes (CSC), each protomer, according to recent work, comprising a trimer of
44 Cellulose Synthases (CESAs)^{11,12}. In the current model, each CESA secretes a glucan chain, resulting in an
45 elementary fibril secreted by a CSC that is composed of 18 glucan chains. It has been shown that the
46 mature CSCs, upon delivery at the plasma membrane, associate with cortical microtubules *via*
47 intermediary partners such as Cellulose Synthase Interactive protein-1 (CSI), which then guide the
48 direction of cellulose synthesis *in muro*¹³. Although microtubule-guided cellulose synthesis is the most
49 described and well-understood facet of this process, a microtubule-independent pathway has been
50 characterized where CSCs separate from their microtubule track in favor of following an already existing
51 cellulose fiber on the other side of the plasma membrane¹⁴. The latter relies on integrating the newly
52 synthesized fibers into an already existing bundle of microfibrils in the cell wall, also hinting towards a
53 mechanism where the motile force of the CSCs is not cytoskeleton-dependent but rather propulsion due
54 to cellulose crystallization¹⁵. A cohort of studies showed that the orientations of the cellulose fibers are
55 consequential to the shape of a cell¹⁶⁻¹⁹ and the existence of a mechanical feedback loop where the cell is
56 able to sense mechanical cues through its cortical microtubular network and adapt the cellulose fiber
57 patterns in the cell wall²⁰.

58 While the cellulose fibers are thought to be the main load-bearing structures in the cell wall, pectins and
59 hemicelluloses interact with them in ways still not fully understood. Hemicelluloses are currently
60 hypothesized to tether cellulose bundles together and form load-bearing hotspots^{21,22}. Pectins, mainly
61 homogalacturonans (HGs), making up to 60% of the dry weight of the primary cell wall⁴, are hypothesized
62 to surround all other components and act as a matrix⁸. Composition, methylation state, and calcium levels
63 have been shown to change the mechanical properties of pectins by altering the level of crosslinking^{23,24}.

64 Despite our knowledge of the chemical composition of the cell wall and of the diversity of the individual
65 components, structural understanding of their secretion and interaction in the cell wall is underexplored.
66 Cellulose-specific stains have been applied directly to live tissue to observe the cellulose fibers and follow
67 their fate during cell elongation^{18,25}, but light microscopy does not offer the necessary resolving power to
68 observe the cellulose fibers and their partners at nanometer resolution. White onion (*Allium cepa*) abaxial
69 epidermal cell wall peels have been used in conjunction with high-resolution Atomic Force Microscopy
70 (AFM) and field emission scanning electron microscopy to characterize the organization of the cell wall
71 components at higher resolution^{9,20,22,26,27}. Despite the knowledge gained, AFM can only access the
72 superficial layers of the cell wall leaving the rest of this polylamellate structure, estimated to be as much
73 as 100 layers, unobserved. Having access to the depth of the cell wall allows a better structural
74 understanding of the cell wall and its relation to cell shape. Here we used Cryo-Focused Ion Beam milling
75 (cryo-FIB-milling) followed by cryo-Electron Tomography (cryo-ET) to observe plunge-frozen *Allium cepa*
76 abaxial periclinal cell walls of onion scale epidermal cells throughout their depth, in near-native
77 conditions.

78 The high-resolution data we gathered at multiple depths of the cell wall reveal the coexistence of cellulose
79 fibers and a structure coined “meshing”, which our data suggest is made at least in part of
80 homogalacturonan pectins. The fibers are shown to adopt a bimodular angular distribution creating layers
81 of fibers of alternating angles of $\pm 45^\circ$ relative to the cell’s long axis.

82

83 **Results**

84 Cryo-ET on epidermal cell wall peel lamellae allows the visualization of the plant cell wall in near-native 85 conditions

86 White onion cell wall peels from the concentric scales, numbered #1 (outermost and oldest scale)
87 inward to number 8 (innermost youngest scale), were generated as described previously (Figure 1A-C)
88 ^{28,29}. They were then flash-frozen and cryo-FIB milling was performed on the periclinal cell walls to produce
89 lamellae ~200nm in thickness, allowing access to the deeper layers (Figure 1D-H). As the angle of milling
90 was well defined, it was possible to measure the depth of the tomograms in the cell wall (Figure 1I and J).
91 Keeping in mind the known artifacts visible on the lamellae, such as curtaining, surface ice contamination,
92 and surface gallium streaks (Figure 1K, red arrows, blue asterisks, and red arrowheads, respectively),
93 tomographic data acquired in this way allowed visualization of the organization of the different elements
94 in the cell wall at high resolution, in near-native conditions. Fields of fibers organized in arrays (Figure 1L,
95 colored arrows) were observed, as well as small, intercalated patches of thin, reticulated densities we
96 term “meshing” (Figure 1L, blue circles and Fig. 2). At the same time, we found the meshing to intercalate
97 between bundles of cellulose fibers (Figure 2A-D, yellow and blue arrows and dashed line, respectively
98 and supplemental video 1). Because manual segmentation of these two features was impossible, two
99 Convolutional Neural Networks (CNN) were trained to recognize these two features using the EMAN2
100 software³⁰. The fiber detection CNN, being very specific, yielded precise maps of the fibers (Figure S1A-C).
101 However, the meshing detection neural network also detected the fiber densities in the tomogram. To
102 circumvent this issue, subtraction of the CNN fiber map from the meshing-CNN map was performed,
103 which assumes that all densities that are not fibers are associated to the novel meshing (Figure S2). The
104 meshing is seen accumulating in patches between the fibers and connecting the fibers together. X-Z cross-
105 sections of the segmentations corrected for lamella tilt allows qualitative assessment of the distribution
106 of these two features within the volume (Figure 2E). In tomograms with a similar layout as in Figure 2A,
107 the volume occupancy of the meshing versus that of the fibers ranged from 30% to 75% (Figure 2F).

108 Fibers travel straight and horizontally in the cell wall and adopt a bimodal angular distribution

109 To produce a vector representation of the fibers suitable for geometrical analysis, a template-
110 matching strategy using the Amira TraceX add-on³¹ was used on the fiber-CNN maps (Figure S1C-F).
111 The following results were extracted from a total dataset of 31 tomograms acquired across the onion
112 scales #2, 5, 6, and 8 (Figure 1A, see supplemental table 1 for a precise description of the data and
113 samples). The density distribution of the orientation of the fibers was analyzed for each tomogram. 26
114 out of the 31 tomograms considered showed a bimodal distribution (Figure 3A and B, supplemental video
115 2), the 5 others exhibited a unimodal distribution (Figure S3D). All the tomograms displaying a bimodal
116 distribution had very similar angles to the long cell axis, averaging $42^\circ \pm 8^\circ$ ($n = 31$ tomograms) and 135°
117 $\pm 10^\circ$ ($n = 26$ tomograms), showing a difference between the two modes of $\sim 90^\circ$. Since all angles were
118 calculated clockwise, the 135° relative to the cell's long axis is equivalent to a 45° angle counterclockwise
119 (Figure 3B and C). When organized according to the scale number where the tomogram was acquired, the
120 density distributions show very similar modes (Figure 3C), suggesting that this bimodal distribution of the
121 orientation of the fibers is consistent throughout all developmental stages studied. Fibers with the same
122 angle cluster together according to their Z-height within the tomographic volume (Figure 3D), creating
123 horizontal layers of cellulose fibers alternating between 45° clockwise/counterclockwise (Figure 3E).

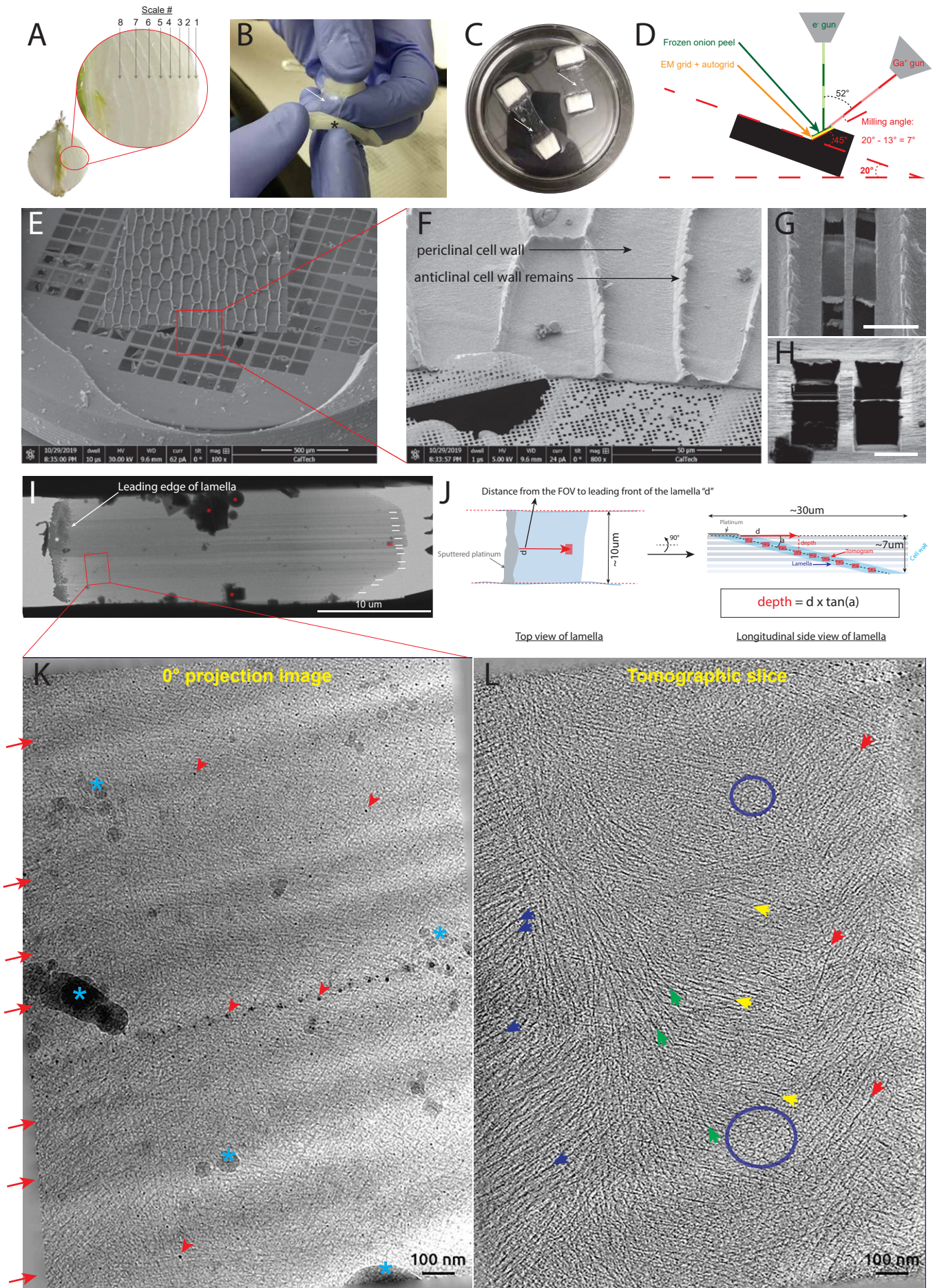


Figure legends

Figure 1 | From fresh onion to reconstructed tomograms

(A) Half-cut onion showing the concentric scales. The inset shows the classic way the scales are numbered, from outermost to innermost. (B) Process of peeling the abaxial epidermal cell wall. (C) Cell wall peels (clear membranes) attached to the two thicker handles (white) incubating in HEPES. (D) Diagram of the SEM chamber and the position of the onion cell wall peel (green) relative to the FIB and electron beam. (E) SEM overview of a cell wall peel laid on an EM Quantifoil grid. (F) Magnified view of the red box in (E) showing the anticlinal and periclinal cell walls (where the milling was done). (G) SEM overview of two final lamellae milled in periclinal cell wall. (H) FIB view of the two same lamellae shown in (G). (I) TEM overview of a milled lamella. Curtaining is visible (white lines) and contamination is seen on the lamella (red asterisks). (J) Left, diagram of a lamella top view showing how the distance d from tomogram to leading edge of lamella is measured. Right, side view of a lamella illustrating how tomograms distributed along the length of the lamella can sample the different layers of the cell wall. (K) 0° projection image of the red boxed area in (I), 0.40 μm below the surface of the cell wall in scale #6. Various typical FIB milling artefacts are visible: curtaining (red arrows), platinum projections (red arrowheads), ice contamination (blue asterisks). (L) Central tomographic slice of the same area shown in (K). Numerous fibers are visible (blue, green, yellow, and red arrows) and small patches of short rod-like, branched densities can be seen between the fibers (blue circle).

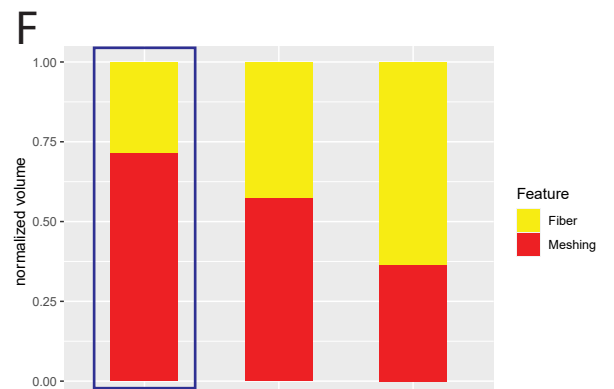
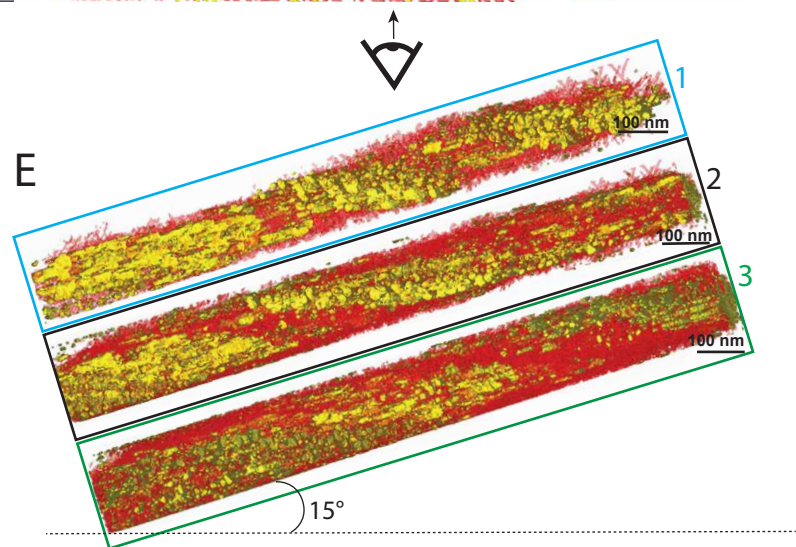
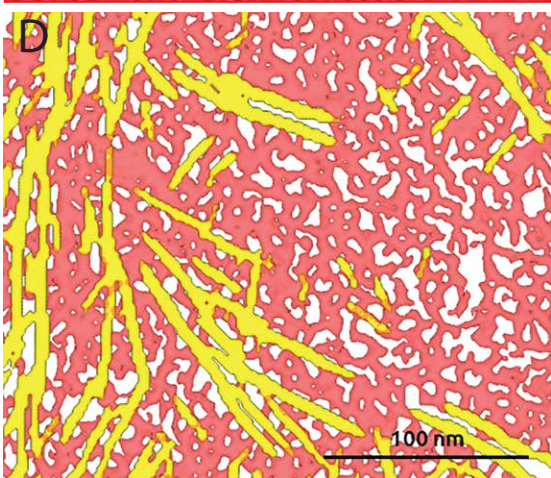
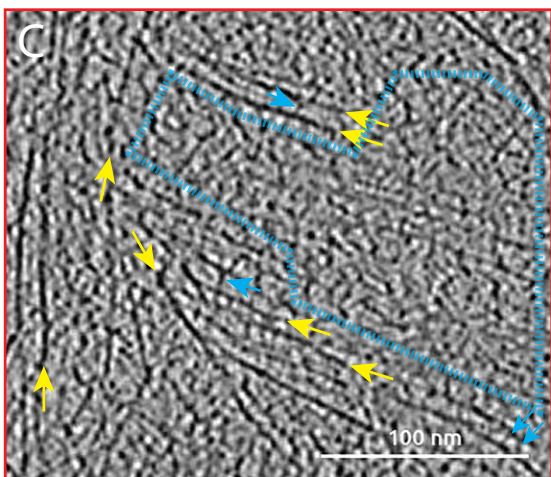
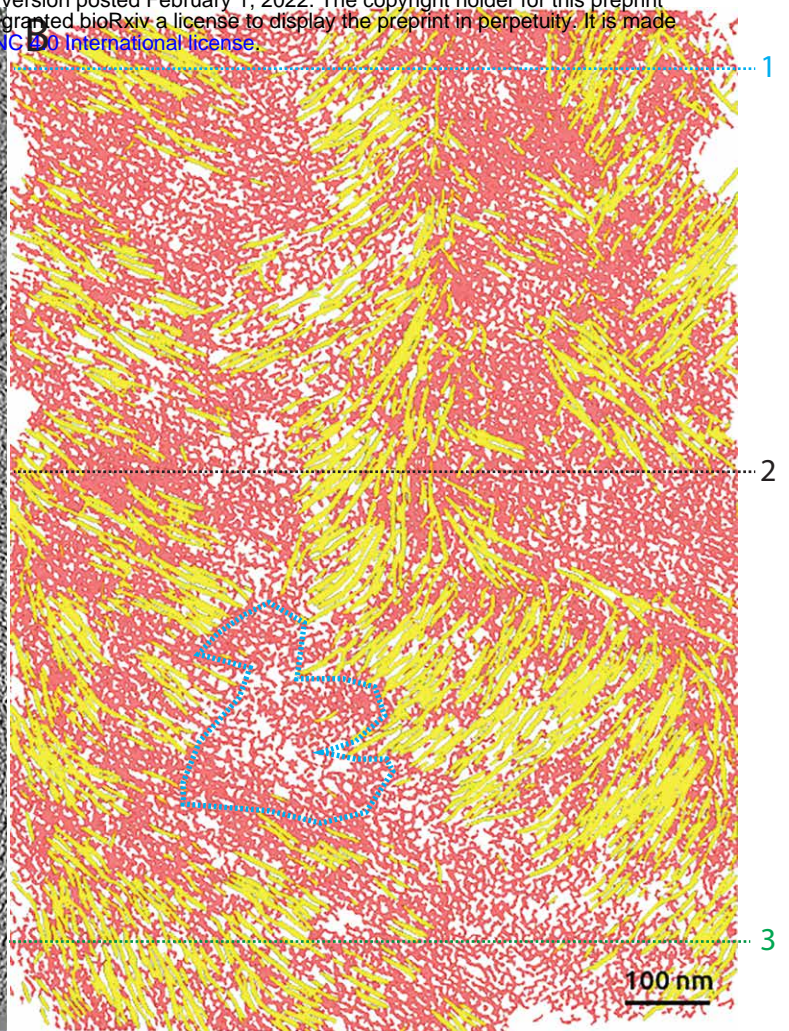
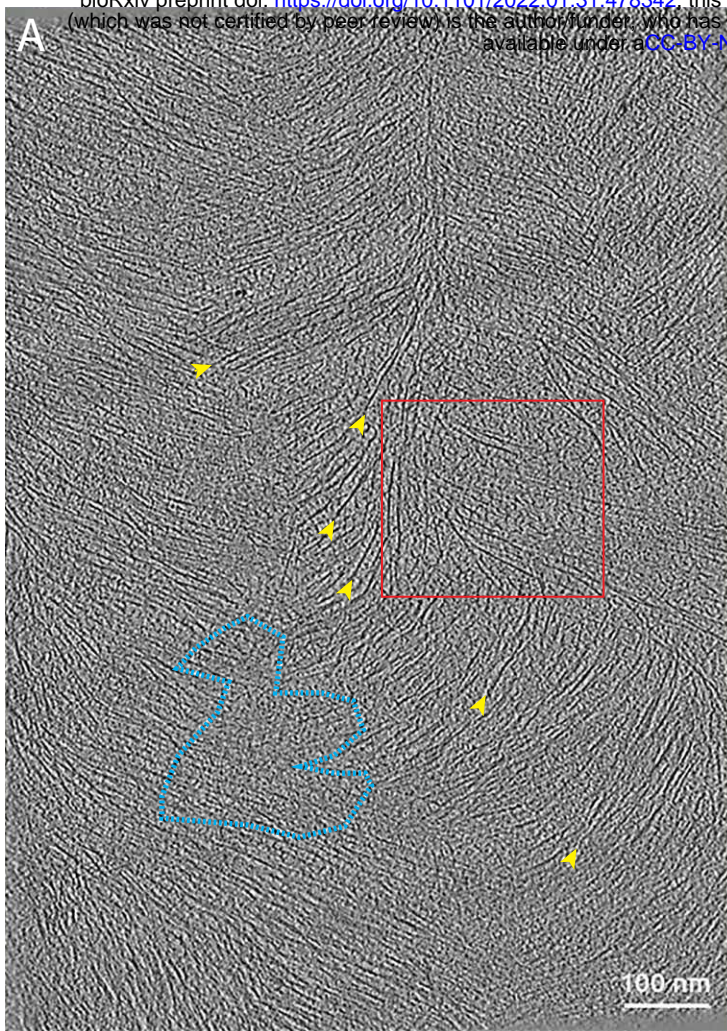


Figure 2 | Two features in tomograms of onion cell walls

(A) Tomographic slice showing fibers (yellow arrowheads) and the filling material in between the fibers (blue circles), the meshing. This tomogram originates from scale #6, 0.64 μm below the surface of the cell wall. (B) CNN segmentations of the fibers (yellow) and the meshing (red). (C) Magnified view from the red boxed region (A) showing fibers (yellow arrows), tethers between the fibers (blue arrows), and patches of meshing (blue dashed region). (D) CNN segmentation of the magnified region. (E) Transverse views at different Y-levels of the segmented volume shown in (B). Tilting is correction for the inclination of the lamella relative to that of the wall. Alternations of fibers (yellow) and meshing (red) are observed. (F) Relative occupancy of fibers vs. meshing in 3 tomographic volumes equivalent to the one shown in this figure (blue squared column is the tomogram shown).

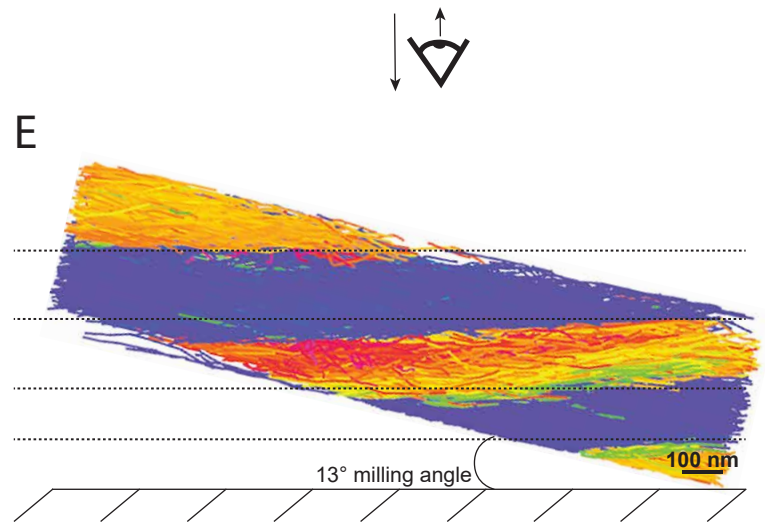
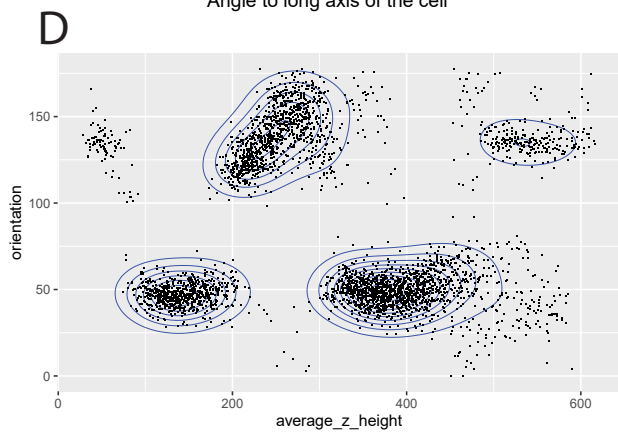
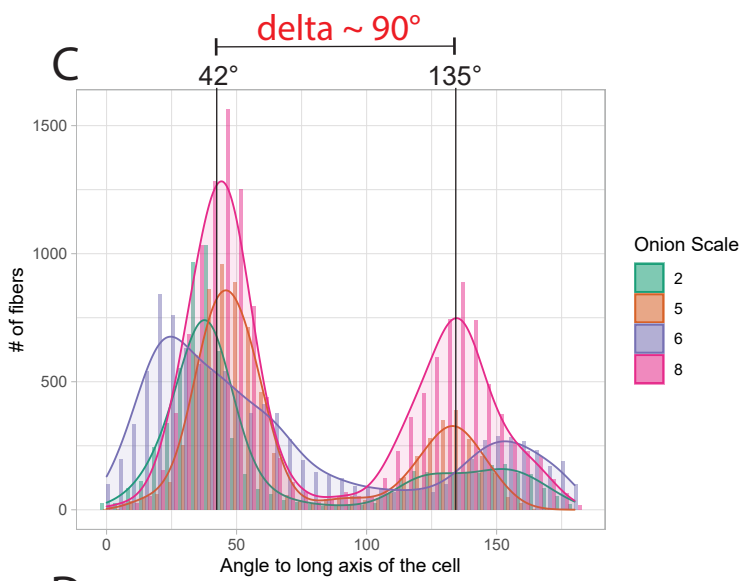
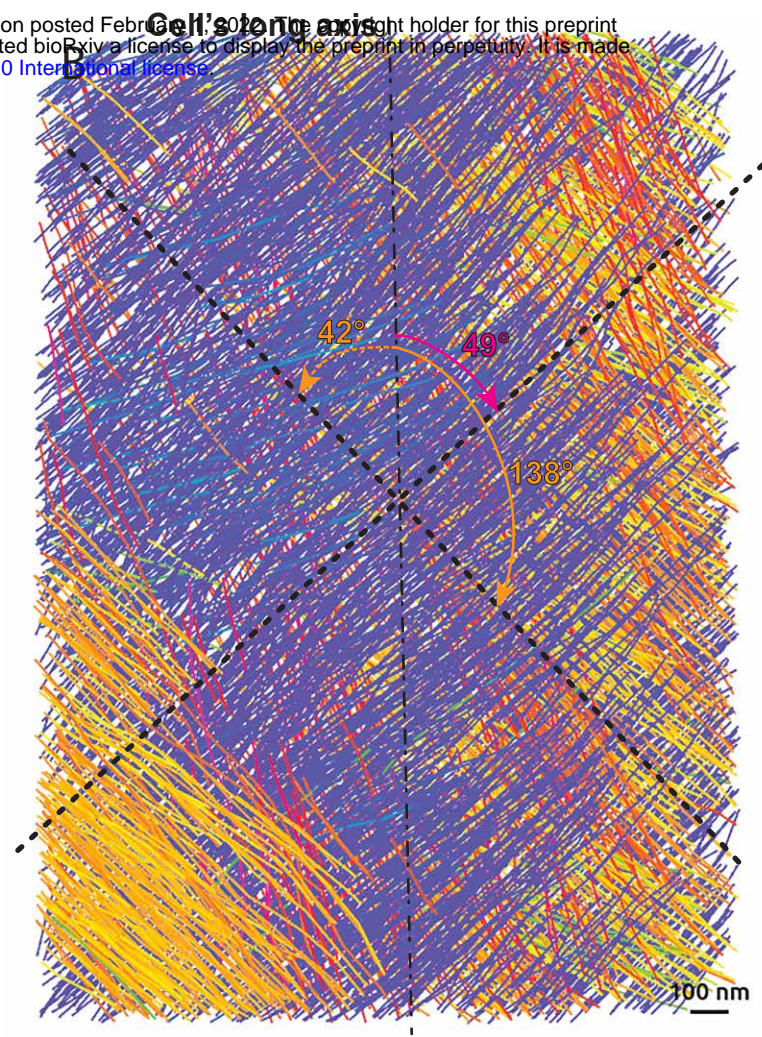
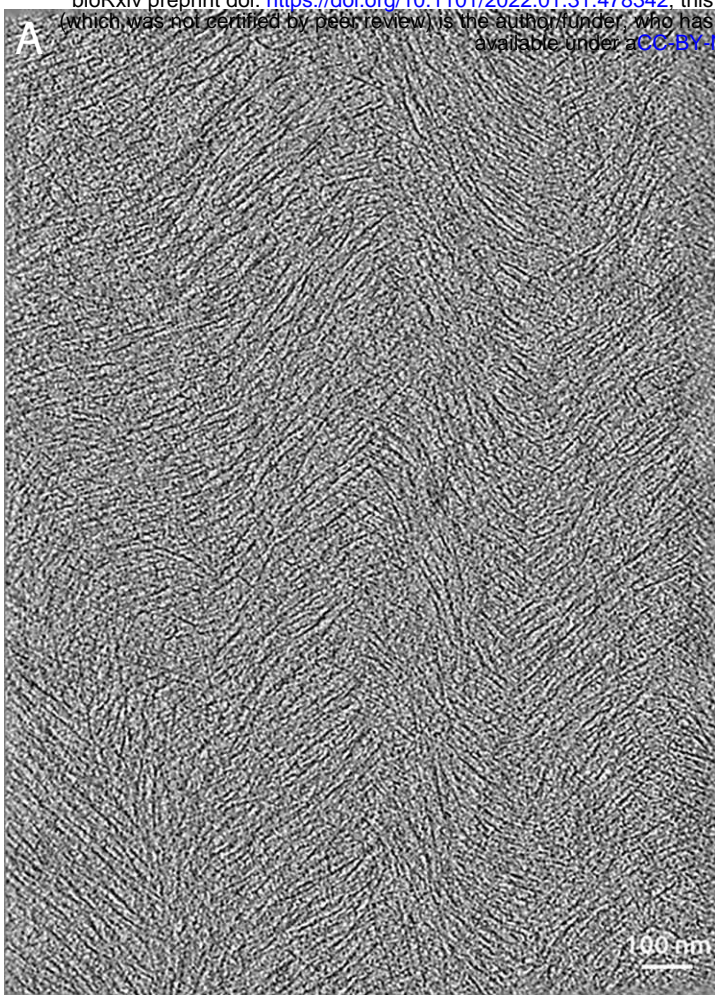


Figure 3 | Cellulose fibers organize in a bimodal angular pattern

(A) Tomographic slice of the cell wall from scale #8, 3.36 μm below the surface. (B) Automated segmentation of the volume shown in (A). Color coding is according to the clockwise angle of the fiber relative to the cell's long axis (\sim vertical dashed line). The two dashed crossed lines indicate the two main angular modes in this volume. They are 49° and 138° . The latter is equivalent to a 42° counterclockwise angle. (C) Distribution plot of the angle of the fibers relative to the cell's long axis by scale number. The 42° and 135° angles correspond to the global modes, aggregating all fibers from all scales. The difference between these two modes is $\sim 90^\circ$. (D) Scatterplot of angles of fibers vs. their average height in the tomographic volume shown in (A) and (B). (E) Bottom cross-sectional view of the segmented volume shown in (B).

124 Three more distribution patterns were observed in addition to a perfectly staggered pattern (Figure 3D
125 and Figure S3A): Overlapped (12 out of 31 tomograms), with fibers of both modal angles mixed at all
126 heights of the tomographic volume (Figure S3B). Staggered-overlapped (9 out of 31 tomograms), similar
127 to the staggered pattern but with overlapping (Figure S3C). Unimodal (5 out of 31 tomograms), with only
128 one modal angle, (Figure S3D).

129 The effect of the depth in the cell wall and the aspect ratio of the cell on the angular distribution was
130 investigated on a per-scale basis. The bimodal angular pattern is found throughout all scales studied (#2,
131 5, 6, and 8), at all depths and cell aspect ratios where data were acquired (Figure S4A-C). The aspect ratios
132 of the milled cells fell into the ranges measured from the light microscopy montages. The average aspect
133 ratios for scales 2, 5, and 8 and their standard deviation overlap strongly (4.3 ± 1.9 , 3.8 ± 1.5 , and $4.1 \pm$
134 1.7 , respectively), suggesting that there is little to no change in the cell's aspect ratio as the scale is pushed
135 outward during growth of the onion (Figure S4D and E).

136 The straightness and the horizontality (relative to the horizontal plane of the cell wall) of each fiber were
137 also analyzed by computing the average radius of curvature and average slope of each fiber, respectively
138 (see methods for details on the computation of these parameters). The average radius of curvature
139 measured throughout all the tomograms is 225 ± 90 nm, which suggests that the fibers are overall straight
140 (Figure S5A and B). The average slope measured throughout all the tomograms is 0.02 ± 0.4 and is
141 centered around 0 (Figure S5C), indicating that the fibers describe horizontal trajectories within the
142 volume of the wall, clearly observable when looking at cross-sections in the segmentations (Figure S5D
143 and E).

144 In summary, these results show that the fibers organize in layers that alternate between $-45^\circ/45^\circ$ relative
145 to the cell's long axis, are relatively straight and travel horizontally relative to the cell wall horizontal plane.

146 The meshing accumulates at the surface of the cell wall

147 We also characterized the meshing, which takes the form of thin and short fibrous densities that either
148 reticulate forming a web-like network (Figure 4A and B) or tether cellulose fibers together (Figure 4C).
149 Tomograms acquired proximal to the platinum layer and thus close to the previous wall interface with the
150 plasma membrane (Figure 4D and J) show extended areas of reticulated meshing (Figure 4E, F, H, and I
151 and Figure 4K, L, N, and O, red and black dashed delineations) accompanied by a reduction in the
152 concentration of fibers. In regions of enriched meshing, the relative volume of the wall region manifesting
153 mesh can be above 50% (Figure 4G and M). Having lamellae milled at an angle allowed probing the
154 structure of the cell wall not only proximal to the cell surface but also more distally in the cell wall (Figure
155 5A). We were therefore able to follow the distribution of the meshing within the depth of the cell wall.
156 Proximal to the cell wall inner surface, transition areas could be observed even within a single
157 tomographic volume. A sub-region of the tomogram was depleted in meshing (Figure 5B, left of the yellow
158 dashed line and supplemental video 3) and contained ordered bundles of fibers, while the other sub-
159 region was enriched in meshing (Figure 5B, D and E and supplemental video 3) and exhibited more
160 disordered arrays of fibers. In contrast, tomograms acquired deeper in the cell wall (farther from the
161 plasma membrane) had reduced amounts of meshing and displayed fibers with an increased degree of
162 bundling and order (Figure 5C, F and G and supplemental video 3). Quantitative analysis of the segmented
163 meshing volume to segmented fiber volume ratio shows a gradual decrease in the amount of meshing as
164 a function of depth in the cell wall (Figure 5H).

165 Taken together, these results suggest the meshing is secreted out of the cell, accumulates at the cell wall-
166 PM interface, and reticulates between the fibers of the first layers of the cell wall.

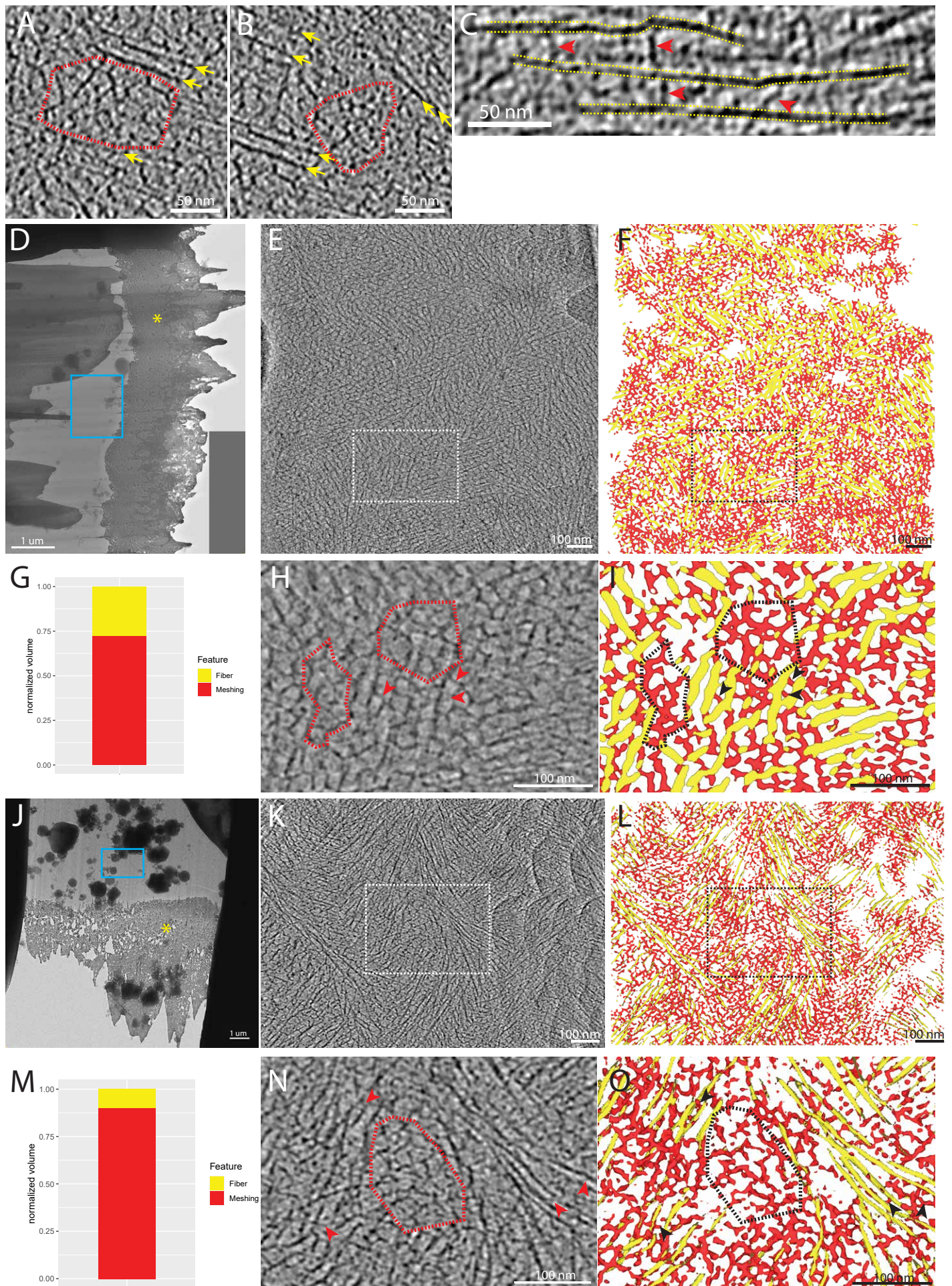


Figure 4 | The meshing is seen in patches and also tethering the fibers together

(A, B) Examples of small patches of meshing (circled in red) surrounded by fibers (yellow arrows). The meshing is characterized by small, branched segments with no particular orientation, creating a reticulated network. (C) Examples of meshing segments (red arrows) tethering fibers together (yellow dashed lines). (D, J) Overviews of lamellae. Yellow asterisk points to the platinum layer. (E, K) Tomographic slices of tomograms acquired near the top of the cell wall (blue rectangle in (D) and (J), respectively) at 0.15 μm and 0.55 μm below the surface, respectively. These tomograms are enriched in meshing as many reticulations can be seen. (F, L) Associated segmentation of the tomographic slice shown in (E) and (K), respectively. Meshing is in red and fibers in yellow. (G, M) Relative quantity of meshing vs. fibers in the tomogram shown in (E) and (K), respectively. (H, N) Magnified views of the white rectangles shown in (E) and (K), respectively. Examples of patches of meshing are shown (red dashed circles) and events of fiber tethering are highlighted (red arrowheads). (I, O) Corresponding segmentation of the magnified view (H) and (N), respectively.

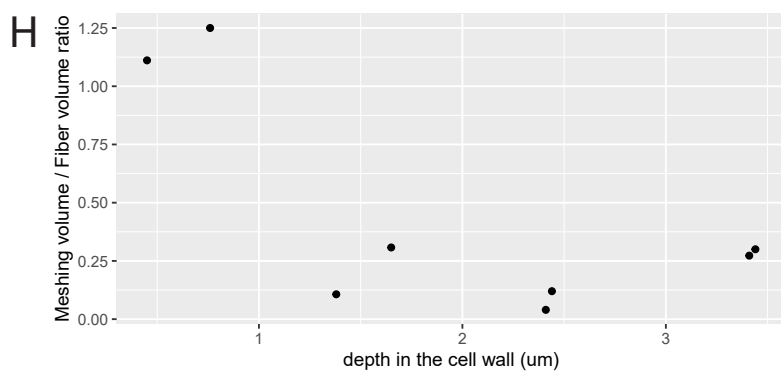
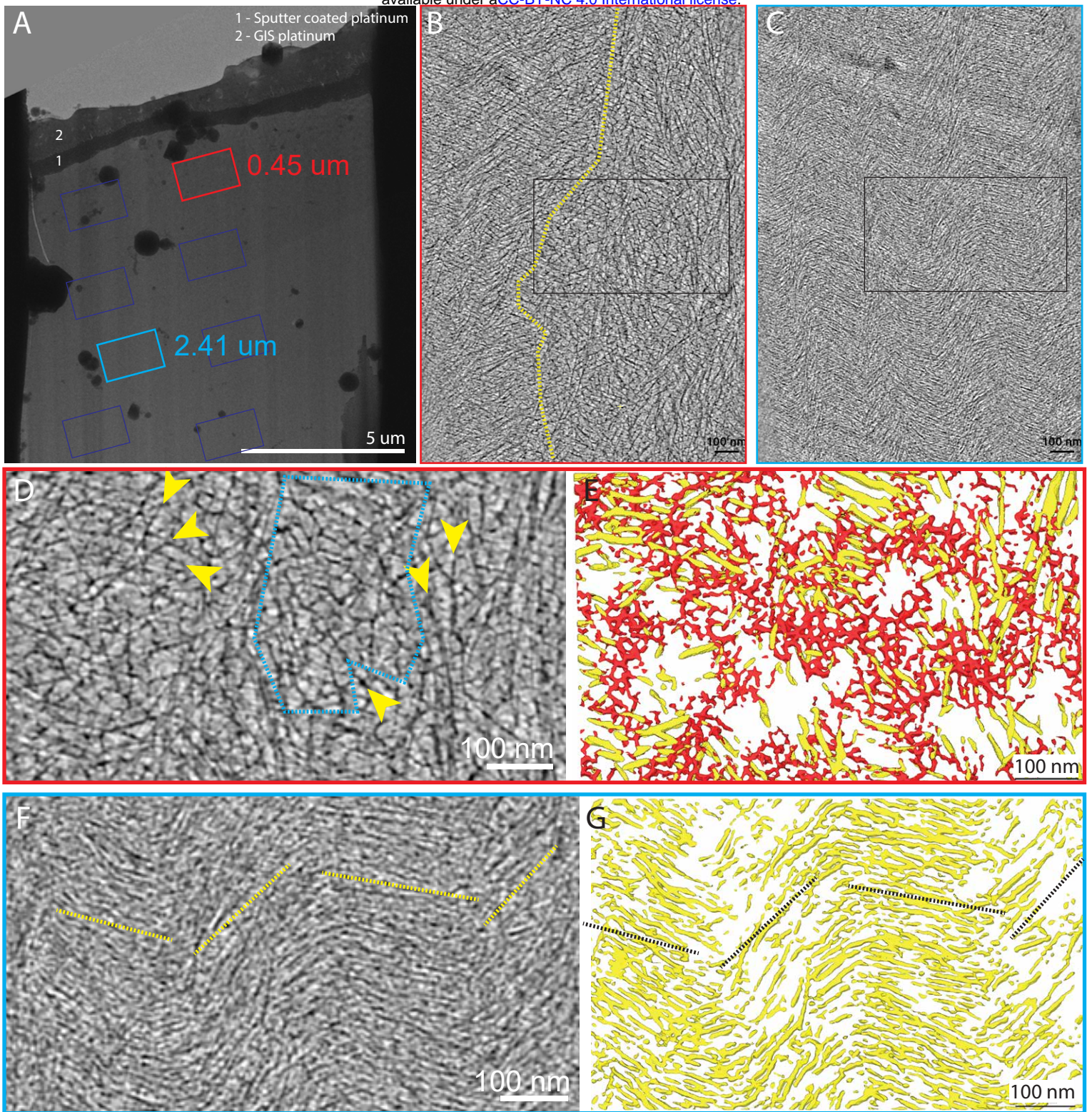


Figure 5 | The meshing is concentrated at the top of the cell wall

(A) Overview of lamella milled in a non-treated cell wall peel from scale #2. Rectangles show where tilt series were acquired. (B) Tomographic slice acquired near the top of the cell wall (red rectangle in (A), at 0.45 μm from the surface). The dashed yellow line indicates the visual limit between an area with a loose network of fibers with a substantial amount of meshing intercalated between the fibers (right of the line), and an area where the fibers seem more bundled together and less meshing is visible (left of the yellow line). (C) Tomographic slice acquired further down the cell wall (blue rectangle in (A), at 2.41 μm from the surface). It shows a denser network of fibers with virtually no visible meshing. (D) Magnified view from the black rectangle in (B). Extensive patches of meshing intercalated with fibers can be observed (blue dashed circle and yellow arrows, respectively). (E) Associated segmentation of the magnified view (D). (F) Magnified view from the black rectangle in (C). Tightly packed fibers with very constant orientations are seen. Yellow dashed lines show the general orientation of the layers visible in this tomographic slice. (G) Associated segmentation of the magnified view (F). (H) Meshing vs. fiber volume ratio calculated from the CNN segmentations in the 8 tomograms extracted from this lamella. The ratios are plotted against the depth from at the tomograms were extracted from the cell wall.

167 Enzymatic digestion of the homogalacturonans alters the morphology and abundance of the meshing

168 We sought to identify the chemical nature of the meshing. According to the literature, pectic
169 homogalacturonans (HGs) make up 50% of the primary onion cell wall³². In the most recent models of the
170 interactions between the different components of the primary cell wall, pectins are thought to surround
171 and tether the cellulose fibers in a calcium-dependent manner^{8,10,23}. Considering this, cell wall peels
172 treated with either BAPTA, a calcium chelator, or *Aspergillus* Pectate Lyase (PL), an enzyme that digests
173 de-methylesterified homogalacturonans, were processed by cryo-FIB milling and cryo-ET to see whether
174 the previously observed meshing would be morphologically altered. The efficiency of the treatments was
175 verified by staining treated and non-treated peels with Chitosan OligoSaccharide Alexa-488 (COS488), an
176 HG-specific fluorescent probe (Figure S6A and B). The decrease in fluorescence (most apparent in the PL-
177 treated material) suggests that these treatments reduce the pectin content in the peels (Figure S6C-F).
178 While applying the onion peels to the EM grids, we noticed that the PL-treated ones seemed to exhibit
179 greatly reduced stiffness. Cryo-SEM images showed a clear difference in the thickness of the peels and a
180 qualitative reduction in the prominence of the bases of the torn-off anticlinal cell walls, suggesting that
181 the specific digestion of demethylated pectins from the cell wall affects cell wall thickness and the
182 continuity between periclinal and anticlinal cell walls (Figure S7).

183 BAPTA-treated cell wall peels show visible meshing, as in untreated walls in increased concentration
184 proximal to the leading edge of the lamella (Figure 6A, C and D, red arrowheads). PL-treated cell wall peels
185 show no meshing at all or remnant densities between the fibers and in small patches that we interpret as
186 partly digested meshing (Figure 6B, E and F). Quantification of meshing volume versus fiber volume as a
187 function of depth of the tomogram in the wall in the non-treated condition clearly shows a gradual
188 decrease (Figure 6G, green dots). The unusually elevated ratio (~9 fold more meshing, Figure 6G black
189 arrow) represented a region of the cell wall ~500nm below the surface (tomogram shown in Figure 4J-O)
190 and was excluded from the computation of the average. The ratios found at the surface of the cell wall in
191 the BAPTA-treated peels show a steady amount of meshing, overall lower than in the same non-treated
192 regions of the cell wall (Figure 6G inset, average ratios of 0.82 ± 0.54 and 1.4 ± 2.2 for BAPTA and non-
193 treated, respectively). In the PL-treated peels, the ratios were much lower (Figure 6G, inset, 0.26 ± 0.27).
194 This suggests that PL treatment reduces the amount of meshing and alters its morphology, indeed in some
195 cases making it practically disappear. Angular distribution of fibers was also assessed in the BAPTA-/PL-
196 treated cell wall peels and the bimodal angular distribution pattern was conserved (Figure 6H).
197 To assess whether the treatments had an impact on the cellulose fiber diameter, averages were generated
198 for each condition (Figure 7A-C) and their cross-sectional thickness were compared by calculating the Full-
199 Width-at-Half-Maximum (FWHM) on the full-length average density profiles. We were not able to
200 measure a significant difference between the three averages generated (5.3, 6.0 and 6.3 nm cross-
201 sectional thicknesses for the non-treated, BAPTA and PL conditions, respectively) (Figure 7D), suggesting
202 the treatments did not alter the diameter of the cellulose fibers.

203

204 Purified pectins reproduce the morphology of wall meshing

205 To test our hypothesis that this meshing network seen around the fibers in the tomograms, altered in the
206 presence of PL, is made of HGs, we imaged purified pectins in aqueous solution. Citrus pectins with an
207 89% content in galacturonic acid (HG) and a degree of methylation of 38% were observed using cryo-ET.
208 As a negative control, solvent only (DI water) grids were also prepared.

BAPTA treated - 0.3 μm
below the surface of the cell wall

Proteinase treated - 0.4 μm
below the surface of the cell wall

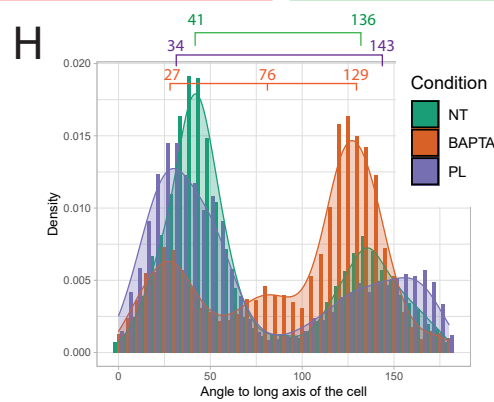
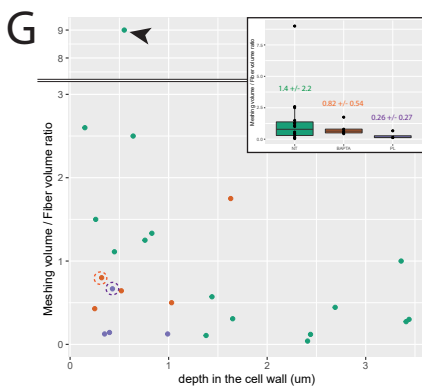
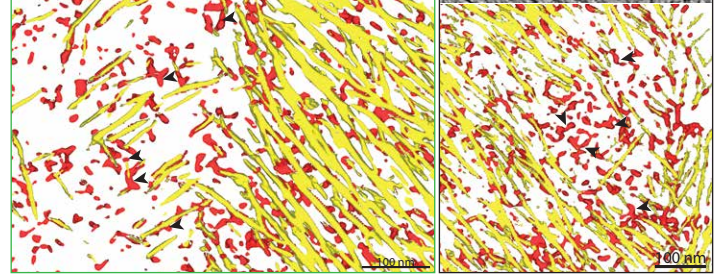
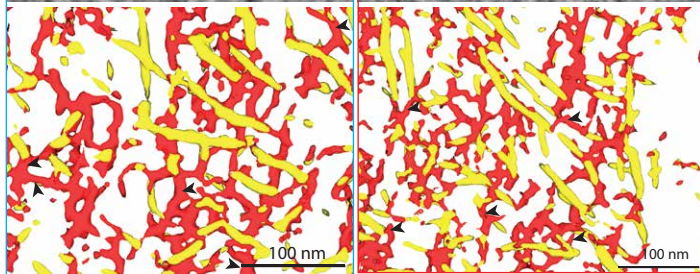
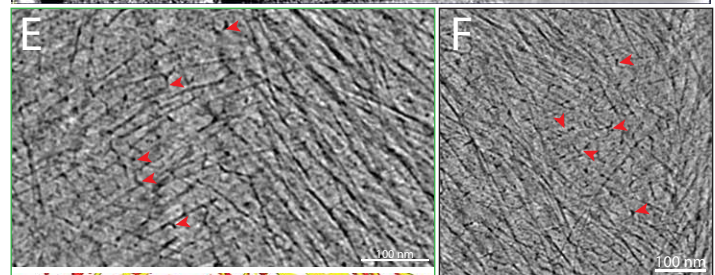
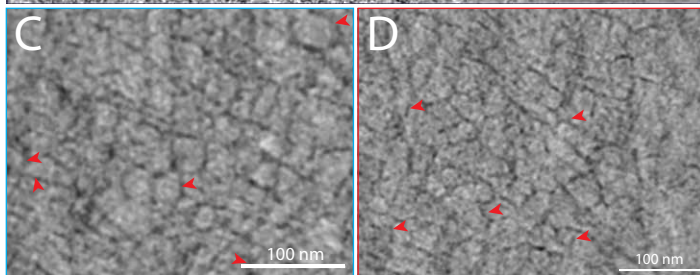
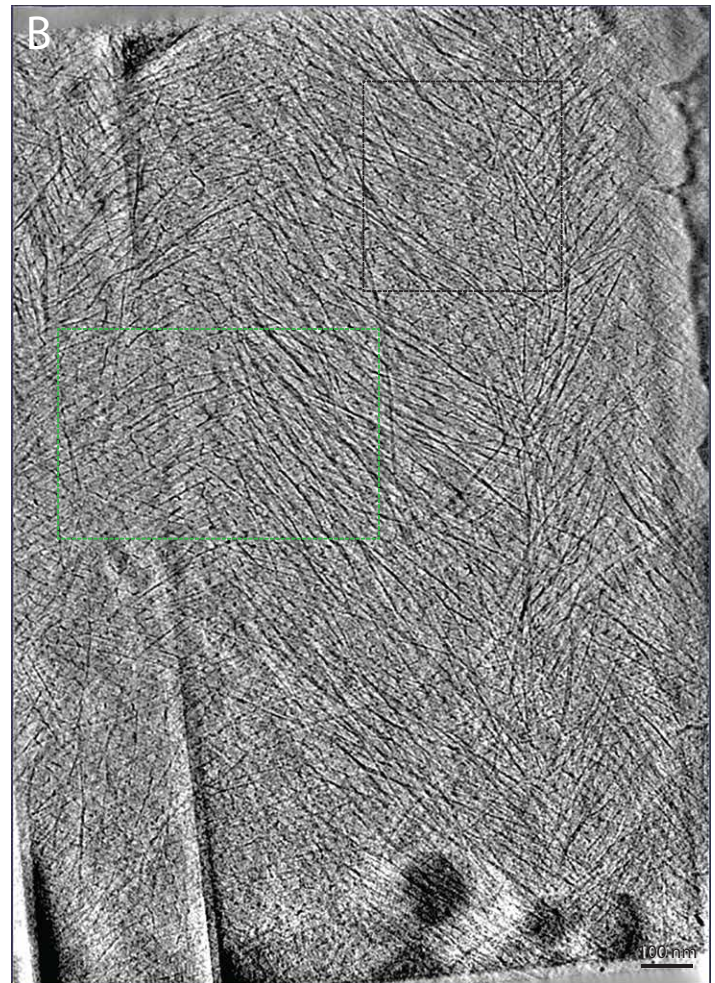
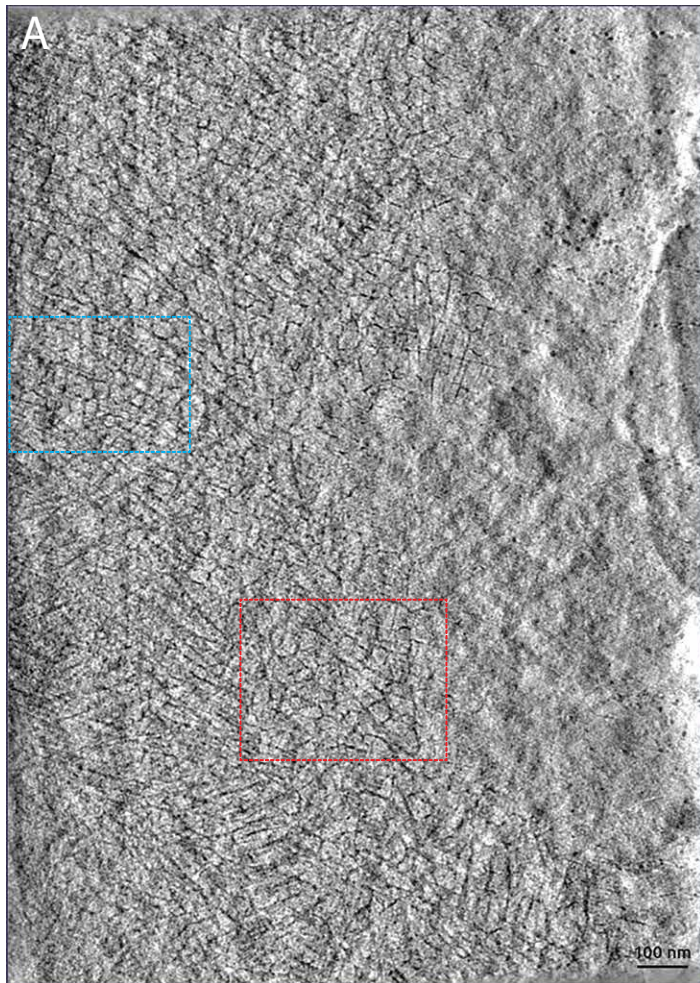


Figure 6 | The morphology of the meshing is affected by pectate lyase but not by BAPTA

(A) Tomographic slice 0.3 μm under the surface of a BAPTA treated cell wall. Meshing patches can be seen among the fibers. (B) Tomographic slice 0.4 μm below the surface of a PL treated cell wall. Meshing remnants can be seen around the fibers. (C, D) Magnified views of areas of the tomogram (blue and red rectangles in tomogram (A), respectively) displaying meshing patches (red arrowheads) with the associated segmentations. (E, F) Magnified views of areas of the tomogram (green and black rectangles in tomogram (B), respectively) displaying small remnant densities in between the fibers (red arrowheads) with the associated segmentations. (G) Meshing vs. fiber volume ratio calculated from the CNN segmentations calculated from 16, 5, and 4 tomograms from non-treated, BAPTA and PL treated peels, respectively. Black arrow points to the unusually high meshing/fiber ratio. The inset boxplot shows the mean meshing/fiber ratio for each condition. The orange and purple dashed circles indicate the data points linked to tomograms shown in (A) and (B), respectively. (H) Distribution plot of the angle of the fibers relative to the cell's long axis by condition. The brackets show the modal values for each of these conditions.

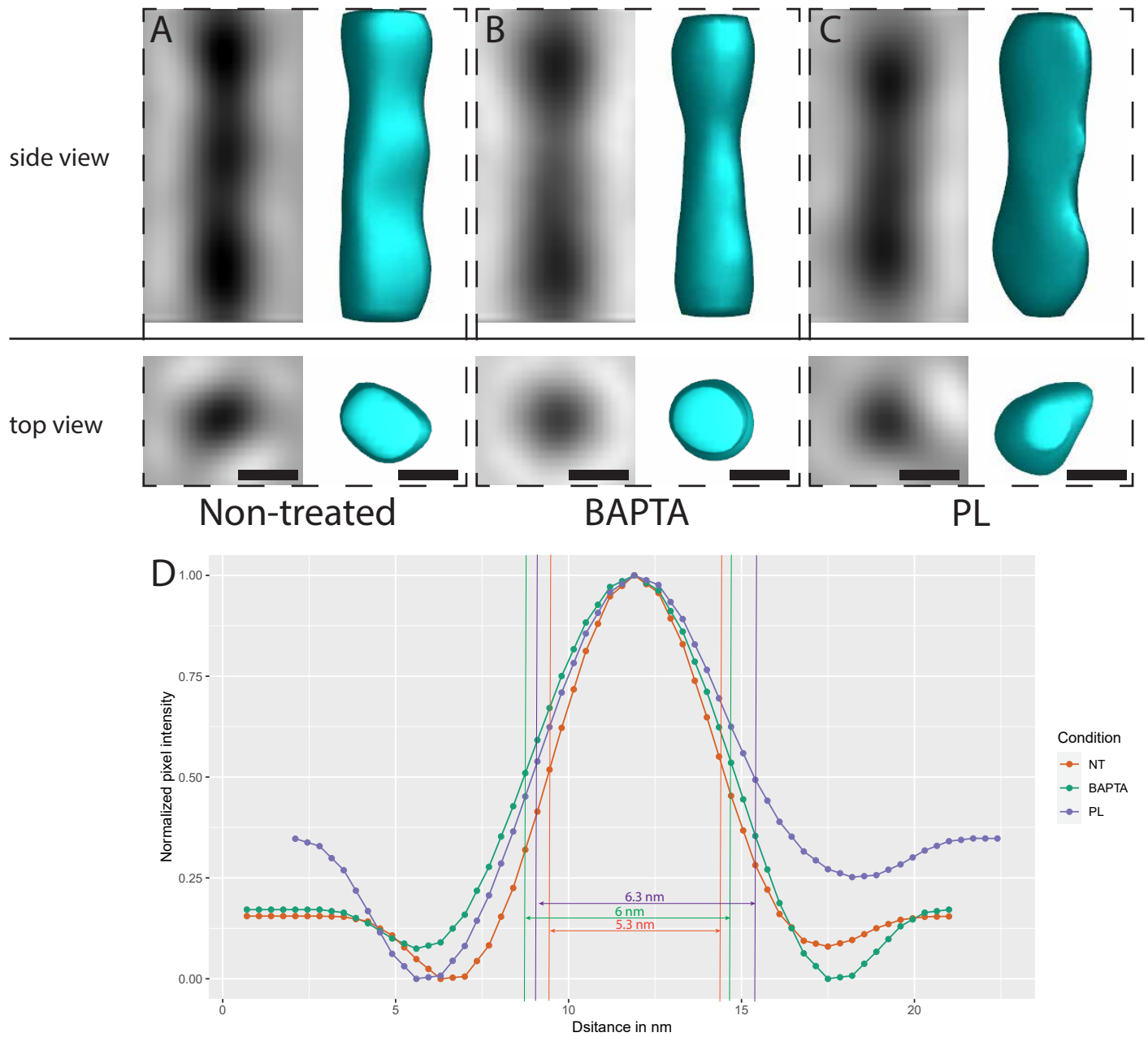


Figure 7 | Fiber averages in non-treated and treated conditions

(A-C) Side views (top panels) and top views (bottom panels) of the fiber averages for the non-treated, BAPTA and PL condition, respectively. Scale bar = 5 nm. (D) Sideview profiles of the averages shown in (A-C) and the FWHM measurements.

209 The latter showed no features (Figure S8A), while the HG solution showed reticulated networks
210 reminiscent of the meshing seen in the native cell walls (Figure S8B).

211 **Discussion**

212 Implications of the bimodal angular distribution

213 A hallmark observation in this work is the remarkable alternation of the cellulose layers between
214 $\pm 45^\circ$ relative to the cell's long axis (90° total angle between successive cellulose layers, supplemental
215 video 2), confirming the crossed-polylamellate organization of the onion primary cell wall^{22,26}. Previous
216 AFM data has observed a similar pattern at the inner surface of the cell walls but only in younger scales
217 (8^{th})²⁸. Along with the measurement of the aspect ratios at the different scales, Kafle et al. suggest that
218 the anticlinal abaxial epidermal cells, as they expand and the scale ages, gradually shift from laying down
219 cellulose fibers with no modal orientation to laying down the fibers in two modal orientations ($\pm 45^\circ$ from
220 the longitudinal axis of the cell), and finally in one modal orientation (90°), therefore linking the aspect
221 ratio of the cell directly to the orientation of the fibers in the inner layers of the cell wall. Our observations
222 show that the $\pm 45^\circ$ bimodal angular distribution is found ubiquitously at all the scales studied (Figure 3C),
223 at all depths of the cell wall and all aspect ratios of the cells observed (Figure S4A and B).

224 Additionally, our light microscope observations of cell wall peels from different scales (Figure S4D and E)
225 show different average aspect ratios and distributions than reported in Kafle et al. 2013 (aspect ratios for
226 scales 2, 5, 8, and 11 of 5.2 ± 0.4 , 2.6 ± 0.1 , 3.4 ± 0.1 and 2.9 ± 0.1 , respectively). This difference can be
227 explained by how the analysis was conducted. Where we performed the measurements on several
228 thousands of cells (Figure S9) in 3 independent onions, Kafle et al. measured the aspect ratio in ~ 100
229 manually selected cells, potentially leading to more bias. There may also be a difference in the onions
230 used, as the source was not genetically characterized in both cases.

231 Our ability to reach the deeper layers of the cell wall allowed observation of the bimodal angular
232 distribution pattern throughout the whole depth of the cell wall (Figure S4A), suggesting there is no
233 gradual reorientation of the cellulose layers as the cell expands, contrary to what has been observed in
234 *Arabidopsis thaliana* root epidermal cells from the elongation zone¹⁸ - as might be expected of cells where
235 the aspect ratio does not substantially change with growth.

236 Layering patterns

237 The case of layers of cellulose fibers stacked on each other, which we termed "staggered" (5/31
238 tomograms, Figure 3D and Figure S3A), was not the only one encountered. "Overlapped" instances (12/31
239 tomograms, Figure S3B) where the layers were fully intertwined with each other, and
240 "Overlapped/staggered" instances (9/31 tomograms, Figure S3C) where the layers were stacked but were
241 also partially overlapping suggests that multiple factors influence the trajectories of the Cellulose
242 Synthase Complexes (CSCs).

243 In the light of our observations, we suggest that microtubule guidance can initiate a new layer with a
244 different orientation from the previous one, which can then be maintained and reinforced by the
245 microtubule-independent cellulose guidance acting as a positive feedback mechanism¹⁴. Creating cleanly
246 staggered alternating layers of cellulose $\pm 90^\circ$ from each other would require very drastic switches
247 between these two guiding modes.

248 This can either be done by a complete synchronous turn-over of the present CSCs in the plasma
249 membrane, which has been measured to require 8 minutes³³, a cessation of cellulose synthase activity
250 that is known to be regulated through phosphorylation^{34,35} or a sudden upregulation of CCs and CSI1
251 translation or delivery to the plasma membrane to redirect the active CSCs to reattach to microtubules so
252 as to create a layer at a new orientation. It remains to be determined how the angles of -45° and $+45^\circ$ are
253 conserved throughout the cell wall. Overlapped events where a mix of orientations are observed at a
254 given height may indicate areas of the cell wall where this sudden directional switch did not occur or
255 failed, hence the gradual transition. These events are the majority (21 if combining “overlapped” and
256 “overlapped/staggered”), indicating that this is the typical mode of orientation switching. “Monolayered”
257 instances (5/31 tomograms, Figure S3D) highlight areas where the cellulose layers are too thick to be
258 entirely captured in one tomographic volume. Given their frequency, we postulate that this is not the
259 norm. According to our model, an uninterrupted positive feedback or a long-term switch delay could
260 create such layers. What regulates this switch and when it occurs is unknown.

261 The mechanical relevance of a long-range straight fiber structure

262 Our results indicate that the cellulose fibers are generally straight with a mean radius of curvature
263 of 225 ± 90 nm though allowing some bend with the curvature radii of individual fibers being as low as
264 ~ 50 nm (Figure S5A and B). Live imaging of GFP-tagged CSCs in the membrane in Arabidopsis leaf cells
265 showed turning angles ranging from 10° to 90° trajectories¹⁴. Additionally, AFM assays coupled with
266 stretching of onion cell wall peels have shown how some fibers are able to form local high curvatures and
267 kinks under particular mechanical constraints²² while the surrounding ones stay straight. We did not spot
268 kinking events in the raw tomograms but cannot dismiss them as the volumes contained high numbers of
269 fibers. Our segmentation method, using conjunctly CNNs and template matching, turns out to be very
270 efficient for relatively straight fibers. However, we do not believe our method of quantifying the radii of
271 curvature allowed recognition of local kinking events for two reasons:
272 i) we measured the average radius of curvatures of the whole fibers, masking local kinks due to averaging.
273 ii) The search cone used by Amira to trace the fibers on the CNN-segmented fiber maps had an angle of
274 37° , thus limiting its search to tracing within that range, excluding any fibers with kinks $>37^\circ$.
275 iii) The majority of the fibers with low radii of curvature in our segmented volumes were actually tracing
276 artefacts where two neighboring or crossing fibers with different orientations were erroneously
277 connected.

278 It is known that the para-crystalline cellulose fibers can have fluctuating degrees of crystallinity along their
279 length, with regions more crystalline or more amorphous than others. Regions with high crystallinity are
280 associated with mechanical stiffness and, therefore, straightness, while amorphous regions are thought
281 to be more flexible³⁶. The local low bending radii observed in our data and the local kinks observed in
282 previous work²² could correspond to regions of relatively lower crystallinity with an increased amount of
283 amorphous cellulose. Regulating the crystallinity of the cellulose could be an additional means to regulate
284 cellulose fiber stiffness.

285 The latest molecular dynamics model of the cell wall, encompassing prior AFM work, predicts much more
286 cross-linking between the cellulose fibers than observed in our tomograms³⁷, although the AFM work
287 does not distinguish if crossing fibers are interacting or just intersecting on slightly different Z-levels^{22,26,28}.
288 Our cryo-ET reconstructions seem to indicate that the fibers within a layer do not interconnect with each
289 other but rather bundle together in a parallel fashion, tethered by the surrounding meshing (Figure 4).

290 Because of the ability to reposition our volumes in 3-dimensions, we were able to assess how the fibers
291 run horizontally relative to the plane of the cell wall by calculating the slope of the fibers within the
292 volume, 0.02 ± 0.4 on average (Figure S5C-E). Although this is the general assumption, it is to be
293 emphasized that the cellulose fiber most likely comes out of the CSC orthogonally to the plasma-
294 membrane, which means that a redirection of the nascent fiber is necessary for its integration in the cell
295 wall. The movement of the CSCs caused by the crystallization of the fiber¹⁵ coupled with the pressure
296 exerted from the existing cell wall which was shown to guide crystallization¹⁴ can explain the flattening
297 of the fiber orientation and its integration in the cell wall. A similar process is at play in the building of the
298 crystalline-cellulose ribbons in the *Gluconacetobacter hansenii* bacterium, where the proper
299 crystallization of the nascent cellulose fibers requires the proximity of the existing extracellular ribbon³⁸.

300 The meshing gradient and the mechanical properties of the cell wall

301 Tomograms of the near-native cell wall show an interconnected network of meshing and cellulose
302 fibers, confirming the single network model of the primary cell wall^{39,40}. In some instances, overlaying the
303 fiber and meshing segmentations shows clear layering (Figure 2E, supplemental video 1) of the two
304 features. This meshing is therefore not just located at the surface of the cell wall but seems to serve as a
305 matrix between the fibers even in more distal layers of the cell wall. This layering can be achieved by two
306 means: i) alternation of secretion of a meshing and cellulose layer, or ii) the meshing is secreted at a
307 constant rate and the bundling of the cellulose fibers as they are laid down gradually excludes or squeezes
308 the greater part of the meshing out of the cellulose layers. A recent molecular dynamics model proposes
309 that cellulose and pectin layers alternate with each other³⁷. This resembles our observations, with the
310 exception that in the hypothetical model, single-pass cellulose layers alternate with layers of pectic matrix.
311 Our observations do not show alternations of 1-fiber thick layers with meshing, but rather that the
312 cellulose layers can be much thicker (Figure 3E and supplemental video 2) and can vary in thickness. In
313 tomograms proximal to the leading edge of the lamellae, the cell wall adjacent to the plasma membrane
314 displayed increased amounts of meshing (Figure 5D-O) in the form of extensive patches. This is consistent
315 with previous AFM work that identified a layer of “meshwork” interfacing between the plasma membrane
316 and the first layers of cellulose fibers of the cell wall²⁶ that disappeared upon treatment with pectate
317 lyase. Because of the topological nature of the AFM technique, the extent to which this meshwork
318 pervades the cell wall could not be assessed. In our experiments, the meshing is detectable until $\sim 1 \mu\text{m}$
319 deep in the cell wall (before the meshing to fiber ratio falls below 0.5, Figure 5H and Figure 6G) as smaller
320 patches and inter-fibrillar tethers (Figure 2 and Figure 4A-C). Such organization is reminiscent of previous
321 Solid State Nuclear Magnetic Resonance (SSNMR) results stating that pectins, when dimethyl-esterified,
322 are cross-linked by calcium, form a branched network that establishes contacts with the cellulose fibers
323 on up to 50% of their surface^{39,40}. Following the amount of meshing throughout a given lamella, we
324 measured a relevant decrease of the quantity of meshing in tomograms from ~ 0 to $3.5 \mu\text{m}$ deep in the
325 cell wall (Figure 5H, supplemental video 3). This gradient of meshing suggests it is secreted and
326 accumulated at the cell wall-PM interface and in the inner-surface layers and gradually drops out of the
327 deeper, older layers of tightly bundled cellulose layers following the same exclusion mechanism explained
328 above (Figure 5C). This confines the meshing at the inner-surface of the cell wall, less than $\sim 1 \mu\text{m}$ deep.
329 This model of cell wall build-up implies structurally different Z-regions. In the light of previous data, we
330 can thus link the structure (fiber – meshing connectivity) to the function (stiffness of the cell wall and its
331 ability to stretch) such that different layers of the wall confer different mechanical properties^{39,40}.

332 The plasma membrane-adjacent, younger layers are comprised of a mix of meshing-interconnecting and
333 less-bundled cellulose fibers conferring more stiffness to these inner-layers, potentially allowing for more
334 reversible elastic deformations and preventing irreversible plastic deformation. The more cell-distal, older
335 layers of the cell wall are comprised mostly of tightly bundled cellulose fibers devoid of meshing. These
336 cellulose bundles are non-pectin-crosslinked, therefore loosening the respective layers of the cell wall and
337 potentially allowing them to stretch and undergo irreversible plastic deformation (creep). Our
338 observations highlight the importance of considering the cell wall as a 3-D polylamellate structure to grasp
339 its mechanical properties fully.

340 Treatments affecting the morphology and quantity of meshing suggest the meshing is HG.

341 The visible thinning of the cell wall upon PL treatment (Figure S7D and E) suggests that removal of the
342 major pectin, HG, leads to a collapse of the stacked layers, suggesting that HG acts as a filler, intercalating
343 between the cellulose layers (Figure 2B and E). This is in line with the latest model of how pectins arrange
344 around the cellulose fibers in the onion primary cell wall^{37,40}.

345 The effect of the PL enzyme on the meshing morphology and abundance (Figure 6G), and the fact that
346 this enzyme specifically digests HGs with low degrees of methyl-esterification indicates that the meshing
347 is predominantly composed of demethylesterified HGs. This is also confirmed by the COS488
348 homogalacturonan-specific staining patterns upon PL treatments (Figure S6D-F). Moreover, the
349 reticulated networks of purified HGs with a ~40% methyl-esterified composition have nearly identical
350 morphology (Figure S8) to what was observed *in situ* in native cell walls, adding plausibility to the proposal
351 that HG is the major component of the meshing. This is consistent with previous observations, showing
352 that digestion with the same pectate lyase enzyme leads to the disappearance of the interfacial pectin
353 between the cell wall and the plasma membrane²⁶.

354 HGs interact strongly with divalent cations like calcium. Specifically calcium ions have been shown to
355 cross-link demethylated HGs, leading to a shift in mechanical properties²³. In the light of this, treatment
356 with BAPTA, a divalent cation chelator, was expected to reduce reticulation. In our data, upon BAPTA
357 treatment, we can still see the branched meshing (Figure 6A, C, D, and G), indicating that maintenance of
358 this structure does not depend on calcium concentration and that branching can still occur in low-calcium
359 concentrations.

360 Overall, our results regarding the nature and distribution of the meshing throughout the cell wall
361 suggest that it consists of demethylesterified HGs. This fits well with the current understanding of pectin
362 biosynthesis where pectins are synthesized in a methylated state in the Golgi Apparatus and
363 demethylated *in muro* by endogenous methylesterases^{24,41,42} and strongly interact with the cellulose
364 fibers³⁹, participating in the stiffness of the primary cell wall⁴⁰.

365 The remnants observed in one instance (Figure 6B, E and F) could be more complex pectic polysaccharides
366 such as rhamno-galacturonan-II, or the hemicellulosic component xyloglucan, shown to coat the cellulose
367 fibers, possibly tethering them together as we observed in our tomograms (Figure 4C)²⁷ or HGs with a
368 higher degree of methylation, and therefore little affected by the enzyme.

369

370

371

372 Our measurements of the diameter of the cellulose fibers cannot weight in favor of the 18- or 24- glucan
373 chain model

374 Averaging of the cellulose fiber diameter in the three conditions considered was performed in an effort
375 to 1) get an idea of the cross-sectional diameter of cellulose fibers *in situ* and 2) check whether PL or
376 BAPTA treatments could have an effect on fiber thickness, as it has been reported that other wall
377 polysaccharides coat the cellulose fibers²⁷. Given the difficulty of assessing the width of a density line in
378 cryo-ET because of defocus, we opted for the Full-Width-at-Half-Maximum (FWHM) standardized method
379 (Figure 7D). By this method, we measured fiber diameters ranging from 5.3 to 6.3 nm. PL or BAPTA
380 treatment did not substantially alter the diameter of the cellulose fibers, therefore suggesting that HGs
381 do not coat the cellulose fibers longitudinally. This does not preclude punctual covalent bindings between
382 the HGs and the cellulose fibers, as mentioned in previous models⁴³. Previous reports had measured
383 several hundred fiber diameters in onion walls *in situ* by AFM. The measurements were between 3.5 to 7
384 nm, which falls within the range of our measurements^{26,44}. While an AFM and cryo-EM study favor of the
385 18 glucan-chain model of an elementary fiber involving CSCs made of hexamers of trimers^{11,44}, Solid State
386 NMR indicates the elementary cellulose fiber is composed of 24 glucan chains made by hexamers of
387 tetrameric cellulose synthases³⁹. Our measurement, which averages range from ~5-6 nm, with a maximal
388 resolution of 3.8 nm (Figure S11), do not allow a conclusion one way or the other.

389 Limitations of this study

390 This work represents, to our knowledge, the first report to use cryo-FIB milling followed by cryo-ET to
391 observe the plant cell wall. Despite the high quality of the data achieved in this study, the throughput of
392 the method is limited by the lengthy milling times and the low survival rate of lamellas from milling to tilt
393 series acquisition. Future work will focus on testing other enzymatic treatments, e.g., specifically directed
394 towards hemicelluloses like xyloglucan or combinations of enzymes and assess the impact of the degraded
395 component on the structure of the cell wall in 3-dimensions.

396 Our study focused on the milling of the periclinal cell wall, as due to their geometry as large flat surfaces
397 (Figure 1E and F), they were more amenable to our approach. This does not preclude the feasibility of
398 milling the anticlinal cell walls, even though initial attempts resulted in unstable, very short lamellae
399 unsuitable for cryo-ET. It would be of high interest to visualize the anticlinal cell walls, notably because
400 they constitute interfaces between neighboring cells of the same scale, allowing the visualization of the
401 pectic mid-lamella⁴⁵. Subsequent studies focusing on the anticlinal cell wall might be enabled by the
402 introduction of more powerful ion sources which are expected to render milling through thick slabs of
403 material more feasible⁴⁶. Lastly, while preparing the sample and positioning the cell wall peel on the EM
404 grid, the polarity of the peel relative to the orientation of the onion bulb was not tracked, something to
405 consider for future experiments that would allow comparison of the relative fiber orientation in different
406 scales.

407 **Methods**

408 Onion cell wall peel preparation

409 White onions were purchased the day of or the day prior to the experiments at the local Pavilions
410 supermarket (845 E California Blvd, Pasadena, CA 91106). Peels at the various concentric scales used
411 throughout this work were generated as described in^{28,29}. Briefly, the scales were sliced longitudinally

412 with a sharp knife or razor blade. Then the middle of each slice, where the width is more or less constant,
413 a ~4 cm long piece was cut out. An incision was made with a sharp razor blade approximately 1 cm away
414 from the edge, creating “handles”. Then these handles were used to pull apart the epidermal layer away
415 from the parenchyma of the scale. This resulted in peels about 1 cm in width and 2-3 cm in length. These
416 peels were incubated for at least 20 min in HEPES buffer (20 mM HEPES, 0.1% Tween-20, pH 6.8 with KOH)
417 and remained in it until freezing. Before freezing, each cell wall peel was mounted between slide and
418 coverslip and screened with a table-top microscope equipped with phase-contrast to ensure that the peel
419 had a homogenous surface of cleanly ruptured cells where only the cell wall remained. Phase-contrast
420 allowed visualization of the remaining floppy, jagged-looking anticlinal cell walls, indicating that peeling
421 of the cell wall was successful.

422 Quantification of the aspect ratios of epidermal cells by light microscopy

423 A large montage of the epidermal cell wall peels was acquired by light microscopy using a Nikon 90i
424 epifluorescence microscope. These maps were segmented with ImageJ with the following method (Figure
425 S9): i) out-of-focus cells and folded-over peels were masked out manually to avoid distorted cell
426 segmentations using the polygon selection tool of imageJ and deleting the selected areas (Figure S9A and
427 B). ii) A binary mask was applied on the montages in order to select the outline of the cells, and the
428 resulting mask was gaussian-filtered (2 pixel) and skeletonized (Figure S9C). iii) The “Analyze particles”
429 tool was used to detect closed cells and calculate their aspect ratio (Figure S9D and E).

430 Enzymatic treatments and staining

431 Pectate lyase from *Aspergillus* (Megazyme, 180 U/mg, Cat # E-PCLYAN2) at 4.7U/mL (8uL of stock solution
432 in 5mL of 50 mM CAPS buffer, pH 10)¹⁰ and BAPTA calcium chelation at 2mM (Sigma Aldrich – Cat # A4926)
433 treatments were performed on cell wall peels generated as described above. Treatments were carried out
434 for 3 hours and 10 min, respectively, on the peels.

435 To screen for the effectivity of the treatments prior to vitrification, staining of non-treated, BAPTA- or PL-
436 treated onion peels by a homogalacturonan-specific probe, Chitosan OligoSaccharide coupled with Alexa-
437 488 (COS488) (Figure S6B) was performed based on a protocol provided by Jozef Mravec (personal
438 communication): 1:1000 dilution from the mother solution kindly provided by Jozef Mravec (kept at -20C
439 wrapped in foil) in 50 mM MES buffer pH 5.8 for 15 min. Peels were then washed with DI water 3
440 consecutive times before being mounted between a slide and coverslip and then screened by confocal
441 laser scanning microscopy⁴⁷.

442 Purified pectin preparation

443 Citrus-derived high homogalacturonan content purified pectins were kindly provided by Professor Hans-
444 Ulrich, from Herbstreith & Fox (<https://www.herbstreith-fox.de/en/>): Pectin Classic CU 701 (38% methyl-
445 esterification, 89% galacturonic acid content). 10mL of 2.5% (w/v) aqueous pectic solutions were made
446 (pH 3.4 according to manufacturer’s MSDS sheet). Serial dilutions at 0.25% and 0.125% were then
447 prepared from the 2.5% solution.

448 Plunge-freezing

449 *Onion cell wall peels*

450 The cell wall peels previously incubated in HEPES buffer were laid on a slide with a drop of HEPES buffer
451 to keep the cell wall hydrated. After incubation in HEPES buffer, the peels were mounted in a drop of
452 HEPES on a slide. A tangential light was shined at the peel to increase visibility. If possible, a magnifying
453 glass affixed on a support can be used. Small rectangular pieces (~2 x 3 mm) were cut out of the cell wall
454 peel with a sharp razor blade and carefully dragged on the carbonated side of glow-discharged (15mA –
455 1min) Quantifoil R2/2 NH2 Cu EM grids (EMSdiasum). Plunge freezing was performed with a 60/40 ratio
456 ethane/propane mix and an FEI Vitrobot Mark IV (Thermo Fischer). Humidity was set at 50%, temperature
457 at 20°C. Grids were first manually backblotted for 6 s in order to attach the cell wall peel firmly to the
458 carbon, followed by two autoblottings (front and back) 5 s, maximal blot force (25) and a drain time of 3
459 s.

460 *Purified pectins*

461 5uL of 2.5%, 0.25% and 0.125% purified pectin was pipetted onto Quantifoil R2/2 NH2 Cu EM grids
462 (EMSdiasum) and the grids were plunge frozen at 100% humidity, 20C with a blot time of 4 s, a medium
463 blot force of 10 and a drain time of 1 s.

464 Cryo-FIB milling

465 During the grid clipping stage, prior to milling, orientation of the peel is important, so the long side of the
466 rectangle was positioned parallel to the notch in autogrid holders (Thermo Fisher) machined with a notch.
467 Like this, the shorter side of the anticlinal cell walls are orthogonal to the FIB beam leading to less
468 obstructed areas of the periclinal cell wall and thus more potential FIB-milling targets. Autogrids were
469 placed in a shuttle and inserted into a Versa 3D dual-beam FIB/SEM microscope with a field emission gun
470 (FEG) (FEI) equipped with a PP3000T cryo-transfer apparatus (Quorum Technologies). They were
471 maintained at -175°C at all times by a cryo-stage⁴⁸. To reduce sample charging and protect the sample
472 from curtaining during milling, the grids were sputter-coated with platinum at 15mA for 60 s. Thin lamellae
473 were generated with the gallium ion beam at 30 kV at angles ranging from 10 to 17°. Rough milling was
474 done at high currents, ranging from 0.3 nA to 100 pA, until the lamellae measured 1 µm in thickness under
475 the FIB view. The current was then progressively brought down to 10 pA for the final milling steps until
476 the measured thickness was between 100 and 200 nm Final polishing by tilting the sample 0.5 to 1° to
477 homogenize the lamella thickness was also done at 10 pA. During the whole procedure, imaging with the
478 SEM beam was done at 5 kV and 27 pA. SEM overviews were used to precisely outline and measure the
479 respective aspect ratios (width vs. length) of the milled cells. When In-chamber Gas Injection System (GIS)
480 Pt coating was performed, the needle was set at 26C and flushed for ~10s before injection onto the onion
481 peel. The injection was performed for ~5 s at a distance of +2 mm from eucentric height.

482 Confocal microscopy

483 Confocal analysis of the onion cell wall peels stained with the COS488 stain was performed on a ZEISS
484 LSM880 equipped with Airy Scan and a GaAsP detector. Magnification used was 40x (C-Apochromat
485 40x/1.2 W Korr M27). Channel settings were set as follows and kept constant throughout the conditions
486 screened: For the Alexa 488 channel the excitation Ar laser (488 nm) was set to 0.3% power, the gain was
487 set to ~700 and pinhole was set to ~10 AU with a pixel dwell time of ~2 µs. A GaAsP detector was used,
488 and the detection range was set from 499 to 630 and the 488 main beam splitter was used. Trans-channel
489 was set with a gain of ~450. Z-stacks were acquired with the optimal Z-step defined by the software, 1.55
490 µm.

491 Electron-cryotomography

492 Tilt-series acquisition was performed on a Titan Krios (Thermo Fisher) equipped with a GIF post-column
493 energy filter (Gatan) and a K3 direct detector 6k x 4k (Gatan). Data acquisition was controlled via SerialEM
494 ⁴⁹ with a 3° tilt increment for a total range of $\pm 60^\circ$ or $\pm 50^\circ$, a defocus of $-10 \mu\text{m}$, and a total dose up to 80
495 $\text{e}^-/\text{Å}^2$. No pre-tilt was applied and a bi-directional tilt scheme was used. Tilt series were then aligned via
496 patch tracking with the IMOD package ⁵⁰ reconstructed using weighted back projection and the SIRT-like
497 filter set to 15 iterations.

498 Mapping out tomograms on the milled cells

499 Orientation of the grid is lost during the transfer from the cryo-SEM chamber to the cryo-TEM autoloader.
500 The grid can be rotated and/or flipped over. This necessitated correlating the orientations found in cryo-
501 SEM and the cryo-TEM data. We, therefore, used the high-resolution montage maps of the lamellae as
502 the reference where the different fields of view of the tomograms can be seen (Figure S10A, blue
503 rectangles). Using Adobe Illustrator, the high-resolution TEM montages were correlated with the TEM grid
504 montages and the cryo-SEM-overviews of the lamellae. The latter are flipped and rotated if needed to fit
505 the final orientation in the TEM used for data collection (Figure S10B). Finally, the angle between the X-
506 axis of the tomograms and the long axis of the cell was registered (Figure S10C, blue and red lines,
507 respectively). This ensured the precise knowledge of the long axis of the milled cell within each tomogram
508 (Figure S10D, black dashed line), which in turn allowed the extraction of biologically relevant numbers.
509 Depth of the tomograms in the cell wall was computed using the nominal milling angle as the inclination
510 and the projected distance d between the leading edge of the lamella (top of the lamella, identified by
511 the presence of platinum) and the center of the ROIs for tilt series acquisition (Figure 1J).

512 Sub-tomogram averaging and cross-sectional measurements

513 Sub-tomogram extraction, alignment, and averaging were performed using the Dynamo software
514 package⁵¹. Initial orientations and positions of cellulose fibers segments were determined using
515 geometrical tools for particle picking in Dynamo⁵². Regions of the filaments with minimal bending and
516 overlapping were traced in 4x binned tomograms. Centers of the particles were placed every $\sim 70 \text{Å}$ along
517 the filament. Final sub-volumes were extracted from 2x binned tomograms with a final pixel size of 6.7Å
518 and $40 \times 40 \times 40$ box size. The total number of sub-tomograms ranged from 750 to 1100 for all three
519 datasets. Initial reference for particle alignment was generated by averaging segments with azimuth
520 randomized orientations. Iterative alignment and averaging procedures were performed according to
521 gold-standard in Dynamo. A loose cylindrical mask was applied for the alignment step. The final mask
522 corrected FSC was estimated in RELION3 using a soft-edge mask (Figure S11)⁵³.

523 Measurement of the cross-sectional thickness

524 The *sideview-profile-average* script⁵⁴ was used by tracing an open contour in the middle of the fiber in
525 3dmod. The following parameters were used: step 1 pixel, length 30 pixels, and thickness 10 pixels. The
526 output json files were imported into R. The average pixel intensities were double normalized relative to
527 the lowest and highest pixel values in each profile to compare curves between conditions. The Full-Width-
528 at-Half-Maximum (FWHM) was used by measuring the width of the gaussian bell at 0.5 relative pixel
529 intensity.

530 Tomogram segmentation

531 *Fiber segmentation*

532 Segmentation was performed on filtered tomograms with the default parameters of EMAN2 (low-pass
533 gaussian cutoff of 0.25 and high-pass gaussian cutoff of 5px) and Convolutional Neural Networks (CNN)³⁰
534 were used to recognize the fibers in the tomograms (Figure S1A-C). Training was performed on several
535 tomograms by boxing ~20 positive examples and ~100 negative examples. The positive examples were
536 precisely segmented using a graphical tablet (*Wacom Cintiq 21uX*) and the CNNs were trained with the
537 default parameters except for the learn rate that was increased in some instances to 0.001 instead of the
538 default 0.0001. The outcome of the trained CNN was checked on the boxed particles and if satisfactory
539 the CNN was applied on the tomogram. Eventually, a second round of training was performed with
540 additional boxes from another tomogram from the same dataset or on itself. The resulting CNN map was
541 then carefully examined versus the filtered tomogram to ensure they agreed, and segmentation was
542 specific to the fibers. For tomograms acquired over the same session on the same lamellae, the same CNN
543 was able to generalize well and segment accurately. Tomograms from different datasets and different
544 lamellae usually required retraining a CNN.

545 Satisfactory CNN segmented volumes were then transferred into *Amira* (Thermo Fisher) to perform
546 template matching fiber tracing with the *TraceX Amira* plugin³¹ (Figure S1D-F) in order to model the fibers
547 as a set of connected nodes. To be able to optimize parameters, we reduced the processing time by
548 binning twice (binning 8 total) the CNN maps. The first step, *Cylinder Correlation*, was performed with the
549 following starting parameters: cylinder length of 50 pixels, an angular sampling of 5, and missing wedge
550 compensation was toggled. The diameter of the template (outer cylinder radius) was set to closely match
551 the apparent thickness of the fibers in the tomogram, usually 4 pixels. As advised in the *Amira* user guide
552 section 3.8 on the *XTracing Extension*, the mask cylinder radius was set to 125% of the outer cylinder
553 radius. The outcome was visually checked to see if the fibers were detected correctly and not too many
554 artefacts were generated. Parameters were slightly modified one-by-one if needed to improve the output.
555 The subsequent step, *Trace Correlation Lines* was performed with the following nominal parameters:
556 minimal line length 60 pixels, direction coefficient 0.3, and minimal distance of 2-times outer-cylinder
557 diameter used previously. Minimum seed correlation and minimum correlation are tomogram-dependent
558 parameters. These values were defined on the correlation field by defining the reasonable correlation
559 value range. The minimum seed correlation and minimum continuation quality are the upper and lower
560 limits of the range, respectively. For the search cone, length was set to 80, angle to 37°, and minimal step
561 size was 10%. The outcome was visually checked to see if the fibers were being traced correctly. To do so,
562 we used the *Spatial Graph View* function and checked for artificial fiber trackings. Parameters were
563 modified if needed to enhance fiber detection and reduce false discoveries. Because of the inherent
564 nature of the signal of cryo-ET volumes and their CNN maps, punctate signals would generate and
565 propagate artefactual vertical (parallel to the Z-dimension) lines. These were first selected by using a
566 Tensor XZ and Tensor ZZ visualizer in the *Spatial Graph View* window and identifying the appropriate
567 thresholds. After the coordinates of all fibers were extracted as a .xml file, fiber tracks with values
568 above/below the thresholds were trimmed out.

569 *Meshing segmentation and quantification*

570 The method to output the CNN maps recognizing the meshing is identical to the one used to segment the
571 fibers. We were unable to generate a CNN that could specifically pick up the meshing. Instead, we resorted
572 to training CNNs that could recognize all features in the tomograms and then subtracted this density map

573 with the one generated from the fiber-trained CNN. This allowed isolation of identified features that were
574 not fibers, assuming that everything that is not fiber belongs to the “meshing” feature. This was done
575 using a custom script called *MeshingSubtract* (available upon demand) that relies on IMOD and bash
576 commands. First, the fiber-CNN map was thresholded. The level of the threshold is chosen in order to
577 mask the fibers as accurately as possible. This mask is then subtracted from the meshing-CNN map to
578 create the subtracted meshing map.

579 To quantify the volume occupancy of these two features, the *imodauto* command was used. A threshold
580 of 0 was used on the masked fiber-CNN. For the subtracted meshing map, the threshold was chosen in
581 order to segment as accurately as possible the meshing by comparing with the low-pass filtered
582 tomogram. Both resulting segmentations were joined using the *imodjoin* command and the *imodinfo*
583 command was used to compute the volume occupancy of each segmented feature (the value taken was
584 the cylinder volume).

585 Data extraction

586 Point (containing only point number, x-, y- and z-coordinates) and segment data (containing only point
587 numbers) from the Amira-Avizo (Thermo Fisher) software was exported as tab-delimited files. The
588 `reformat_amira_output.m`⁵⁵, available from <https://schurlab.ist.ac.at/downloads/> was used to convert
589 these files into IMOD formatted tab-delimited text files, which were then further analyzed using custom
590 scripts in python.

591 First, all contours with an out-of-plane angle of larger than 70 degrees were removed, as those did not
592 correspond to fibers but rather to tomogram reconstruction artifacts. For each model, the long axis of
593 the cell was accurately determined as detailed above. Then the model was rotated around the y-axis to
594 reposition the volume according to the angle applied during the milling step and lost during the volume
595 flattening occurring during tomogram reconstruction.

596 To overcome the uneven spacing of points on contours exported from Amira, fiber contours were
597 interpolated using cubic splines resulting in a sampling rate of 1 nm along the length of the fiber. From
598 these reoriented volumes in the cell wall, fiber length, radius of curvature, slope of the fiber, clockwise
599 angle of the fiber relative to the cell’s long axis,

600 The length of individual fibers was calculated as the sum of distances between neighboring points along
601 its run:

$$602 \text{ length} = \sum_{i=1}^{n-1} \text{distance}(\text{point}_i, \text{point}_{i+1})$$

603 With n being the number of points of the given contour representing the fiber.

604 The curvature radius was calculated by averaging the local curvature radii over all triples of neighboring
605 points within a given contour. For this the reciprocal relationship between the Menger curvature and
606 the curvature radius was employed:

$$607 \text{ radius of curvature} \\ 608 = \sum_{i=1}^{n-2} \frac{\text{distance}(\text{point}_i, \text{point}_{i+1}) * \text{distance}(\text{point}_{i+1}, \text{point}_{i+2}) * \text{distance}(\text{point}_i, \text{point}_{i+2})}{4 * \text{area}(\text{point}_i, \text{point}_{i+1}, \text{point}_{i+2})}$$

609

610 With n being the number of points of the given contour representing the fiber.

611 Prior to calculating local slopes along the run of a fiber, the sequence of the points was, if necessary,
612 adjusted so that the first point of the contour would have a lower y-coordinate than the last point of the
613 contour. This was done to establish a common direction for all fibers within a tomogram. To calculate
614 the slope between two neighboring points on a contour representing a fiber the difference between
615 their z-coordinate is divided by their distance in the xy-plane:

616

$$617 \text{ slope} = \frac{\text{value}_z(\text{point}_{i+1}) - \text{value}_z(\text{point}_i)}{\text{distance}_{xy}(\text{point}_i, \text{point}_{i+1})}$$

618

619 With $\text{value}_z(\text{point})$ extracting the z-coordinate of a given point and $\text{distance}_{xz}(\text{point}, \text{point})$ calculating
620 the distance between two points only considering x- and y-coordinates.

621 For calculating the average z-height of a fiber, the z-coordinates of all points in the respective contour
622 were averaged.

623 For calculating the angle between a fiber and the long axis of the cell, the orientation of the fiber was
624 approximated by a vector pointing from its end with the lower y-coordinate value to its end with the
625 higher y-coordinate value. The vector representing the long axis of the cell was calculated from the
626 orientation of the cell on the grid and the rotations applied during tomogram reconstruction.

$$627 \text{ Angle to long axis of the cell} = \text{degree}(\arctan2(\vec{c}_x * \vec{f}_y - \vec{c}_y * \vec{f}_x, \vec{c}_x * \vec{f}_x + \vec{c}_y * \vec{f}_y))$$

628 With x and y representing the x and y scalars of the vectors of the long axis of the cell (\vec{c}) or the fiber (\vec{f}),
629 respectively. The resulting angles in radians were then transformed to degrees as depicted in the
630 figures.

631 Data analysis and visualization

632 All the data analysis, data exploration and statistical analysis was performed with R. Specifically,
633 statistical analysis of the value distributions and modelling was done by the mixed models method using
634 the *dipTest* and *mixtools* R packages.

635 **Acknowledgments**

636 This work was supported by the Howard Hughes Medical Institute (HHMI) and grant R35 GM122588 to
637 Grant J Jensen, and Austrian Science Fund (FWF): P33367 to Florian KM Schur. We thank Noé Cochetel for
638 his GST4 guidance and great help in data analysis, discovery and representation with the R software. We
639 thank Hans-Ulrich Endress for graciously providing us with the purified citrus pectin, Jozed Mravec for
640 generating and providing the COS488 probe. Cryo-EM work was done in the Beckman Institute Resource
641 Center for Transmission Electron Microscopy at Caltech.

642 This article is subject to HHMI's Open Access to Publications policy. HHMI lab heads have previously
643 granted a nonexclusive CC BY 4.0 license to the public and a sublicensable license to HHMI in their research

644 articles. Pursuant to those licenses, the author-accepted manuscript of this article can be made freely
645 available under a CC BY 4.0 license immediately upon publication.

646 **Bibliography**

- 647 1. Bar-On, Y. M., Phillips, R. & Milo, R. The biomass distribution on Earth. *Proc. Natl. Acad. Sci.* **115**,
648 6506–6511 (2018).
- 649 2. Johnson, M. P. Photosynthesis. *Essays Biochem.* **60**, 255 (2016).
- 650 3. Verbančič, J., Lunn, J. E., Stitt, M. & Persson, S. Carbon Supply and the Regulation of Cell Wall
651 Synthesis. *Molecular Plant* vol. 11 75–94 (2018).
- 652 4. Voragen, A. G. J., Coenen, G. J., Verhoef, R. P. & Schols, H. A. Pectin, a versatile polysaccharide
653 present in plant cell walls. *Struct. Chem.* **20**, 263–275 (2009).
- 654 5. Zhang, B., Gao, Y., Zhang, L. & Zhou, Y. The plant cell wall: Biosynthesis, construction, and
655 functions. *Journal of Integrative Plant Biology* vol. 63 251–272 (2021).
- 656 6. Ruel, K., Nishiyama, Y. & Joseleau, J.-P. Crystalline and amorphous cellulose in the secondary
657 walls of Arabidopsis. *Plant Sci.* **193–194**, 48–61 (2012).
- 658 7. Makarem, M. *et al.* Distinguishing Mesoscale Polar Order (Unidirectional vs Bidirectional) of
659 Cellulose Microfibrils in Plant Cell Walls Using Sum Frequency Generation Spectroscopy. *J. Phys.*
660 *Chem. B* **124**, 8071–8081 (2020).
- 661 8. Cosgrove, D. J. Nanoscale structure, mechanics and growth of epidermal cell walls. *Current*
662 *Opinion in Plant Biology* vol. 46 77–86 (2018).
- 663 9. Wang, X. & Cosgrove, D. J. Pectin methylesterase selectively softens the onion epidermal wall 1
664 yet reduces acid-induced creep 2 3 4 Running title: Effects of pectin methylesterase on cell wall
665 mechanics. *J. Exp. Bot.* (2020).
- 666 10. Zhang, T., Tang, H., Vavylonis, D. & Cosgrove, D. J. Disentangling loosening from softening:
667 insights into primary cell wall structure. *Plant J.* **100**, 1101–1117 (2019).
- 668 11. Purushotham, P., Ho, R. & Zimmer, J. Architecture of a catalytically active homotrimeric plant
669 cellulose synthase complex. *Science* (2020).
- 670 12. Nixon, B. T. *et al.* Comparative Structural and Computational Analysis Supports Eighteen Cellulose
671 Synthases in the Plant Cellulose Synthesis Complex. *Sci. Rep.* **6**, 28696 (2016).
- 672 13. Li, S., Lei, L., Somerville, C. R. & Gu, Y. Cellulose synthase interactive protein 1 (CS11) mediates the
673 intimate relationship between cellulose microfibrils and cortical microtubules. *Plant Signal.*
674 *Behav.* **7**, 1–5 (2012).
- 675 14. Chan, J., Coen, E., Chan, J. & Coen, E. Interaction between Autonomous and Microtubule
676 Guidance Systems Controls Cellulose Synthase Report Interaction between Autonomous and
677 Microtubule Guidance Systems Controls Cellulose Synthase Trajectories. *Curr. Biol.* 1–7 (2020).
- 678 15. Diotallevi, F. & Mulder, B. The cellulose synthase complex: A polymerization driven
679 supramolecular motor. *Biophys. J.* **92**, 2666–2673 (2007).
- 680 16. Kuki, H. *et al.* Quantitative confocal imaging method for analyzing cellulose dynamics during cell

- 681 wall regeneration in *Arabidopsis* mesophyll protoplasts. *Plant Direct* **1**, e00021 (2017).
- 682 17. Wang, Y. & Jiao, Y. Cellulose Microfibril-Mediated Directional Plant Cell Expansion: Gas and
683 Brake. *Mol. Plant* **13**, 1670–1672 (2020).
- 684 18. Anderson, C. T., Carroll, A., Akhmetova, L. & Somerville, C. Real-time imaging of cellulose
685 reorientation during cell wall expansion in *Arabidopsis* roots. *Plant Physiol.* **152**, 787–796 (2010).
- 686 19. Aouar, L., Chebli, Y. & Geitmann, A. Morphogenesis of complex plant cell shapes: The mechanical
687 role of crystalline cellulose in growing pollen tubes. *Sex. Plant Reprod.* **23**, 15–27 (2010).
- 688 20. Sampathkumar, A. *et al.* Subcellular and supracellular mechanical stress prescribes cytoskeleton
689 behavior in *Arabidopsis* cotyledon pavement cells. *Elife* **3**, e01967 (2014).
- 690 21. Park, Y. B. & Cosgrove, D. J. A revised architecture of primary cell walls based on biomechanical
691 changes induced by substrate-specific endoglucanases. *Plant Physiol.* **158**, 1933–1943 (2012).
- 692 22. Zhang, T., Vavylonis, D., Durachko, D. M. & Cosgrove, D. J. Nanoscale movements of cellulose
693 microfibrils in primary cell walls. *Nat. Plants* **3**, 17056 (2017).
- 694 23. Cao, L., Lu, W., Mata, A., Nishinari, K. & Fang, Y. Egg-box model-based gelation of alginate and
695 pectin: A review. *Carbohydrate Polymers* vol. 242 116389 (2020).
- 696 24. Shin, Y., Chane, A., Jung, M. & Lee, Y. Recent Advances in Understanding the Roles of Pectin as an
697 Active Participant in Plant Signaling Networks. *Plants* **10**, 1712 (2021).
- 698 25. Bidhendi, A. J. & Geitmann, A. Geometrical Details Matter for Mechanical Modeling of Cell
699 Morphogenesis. *Dev. Cell* **50**, 117-125.e2 (2019).
- 700 26. Zhang, T., Zheng, Y. & Cosgrove, D. J. Spatial organization of cellulose microfibrils and matrix
701 polysaccharides in primary plant cell walls as imaged by multichannel atomic force microscopy.
702 *Plant J.* **85**, 179–192 (2016).
- 703 27. Zheng, Y., Wang, X., Chen, Y., Wagner, E. & Cosgrove, D. J. Xyloglucan in the primary cell wall:
704 assessment by FESEM, selective enzyme digestions and nanogold affinity tags. *Plant J.* **93**, 211–
705 226 (2018).
- 706 28. Kafle, K. *et al.* Cellulose microfibril orientation in onion (*Allium cepa* L.) epidermis studied by
707 atomic force microscopy (AFM) and vibrational sum frequency generation (SFG) spectroscopy.
708 *Cellulose* **21**, 1075–1086 (2013).
- 709 29. Durachko, D., Park, Y. B., Zhang, T. & Cosgrove, D. Biomechanical Characterization of Onion
710 Epidermal Cell Walls. *BIO-PROTOCOL* **7**, (2017).
- 711 30. Chen, M. *et al.* Convolutional neural networks for automated annotation of cellular cryo-electron
712 tomograms. *Nat. Methods* **14**, 983–985 (2017).
- 713 31. Rigort, A. *et al.* Automated segmentation of electron tomograms for a quantitative description of
714 actin filament networks. *J. Struct. Biol.* **177**, 135–144 (2012).
- 715 32. Wilson, L. A., Deligey, F., Wang, T. & Cosgrove, D. J. Saccharide analysis of onion outer epidermal
716 walls. *Biotechnol. Biofuels* **14**, (2021).
- 717 33. Sampathkumar, A. *et al.* Patterning and Lifetime of Plasma Membrane-Localized Cellulose
718 Synthase Is Dependent on Actin Organization in *Arabidopsis* Interphase Cells. *Plant Physiol.* **162**,

- 719 675–688 (2013).
- 720 34. Sánchez-Rodríguez, C. *et al.* BRASSINOSTEROID INSENSITIVE2 negatively regulates cellulose
721 synthesis in Arabidopsis by phosphorylating cellulose synthase 1. *Proc. Natl. Acad. Sci.* **114**, 3533–
722 3538 (2017).
- 723 35. Speicher, T. L., Li, P. Z. & Wallace, I. S. Phosphoregulation of the Plant Cellulose Synthase
724 Complex and Cellulose Synthase-Like Proteins. *Plants* **7**, (2018).
- 725 36. Djafari Petroudy, S. R. Physical and mechanical properties of natural fibers. in *Advanced High*
726 *Strength Natural Fibre Composites in Construction* 59–83 (Woodhead Publishing, 2017).
- 727 37. Zhang, Y., Yu, J., Wang, X., Durachko, D. M. & Zhang, S. Molecular insights into the complex
728 mechanics of plant epidermal cell walls. *Science (80-.)*. **372**, 35 (2021).
- 729 38. Nicolas, W. J., Ghosal, D., Tocheva, E. I., Meyerowitz, E. M. & Jensen, G. J. Structure of the
730 bacterial cellulose ribbon and its assembly-guiding cytoskeleton by electron cryotomography. *J.*
731 *Bacteriol.* (2020).
- 732 39. Wang, T. & Hong, M. Solid-state NMR investigations of cellulose structure and interactions with
733 matrix polysaccharides in plant primary cell walls. *J. Exp. Bot.* **67**, 503–514 (2016).
- 734 40. Phyo, P., Gu, Y. & Hong, M. Impact of acidic pH on plant cell wall polysaccharide structure and
735 dynamics: insights into the mechanism of acid growth in plants from solid-state NMR. *Cellulose*
736 **26**, 291–304 (2019).
- 737 41. Braybrook, S. A. & Peaucelle, A. Mechano-Chemical Aspects of Organ Formation in Arabidopsis
738 thaliana: The Relationship between Auxin and Pectin. *PLoS One* **8**, e57813 (2013).
- 739 42. Goubet, F. & Mohnen, D. Subcellular localization and topology of homogalacturonan
740 methyltransferase in suspension-cultured Nicotiana tabacum cells. *Planta* **199**, 112–
741 117 (1999).
- 742 43. Cosgrove, D. J. Re-constructing our models of cellulose and primary cell wall assembly. *Current*
743 *Opinion in Plant Biology* vol. 22 122–131 (2014).
- 744 44. Song, B., Zhao, S., Shen, W., Collings, C. & Ding, S.-Y. Direct Measurement of Plant Cellulose
745 Microfibril and Bundles in Native Cell Walls. *Front. Plant Sci.* **11**, 479 (2020).
- 746 45. Zamil, M. S. & Geitmann, A. The middle lamella—more than a glue. *Phys. Biol.* **14**, 015004 (2017).
- 747 46. McClelland, J. J. *et al.* Bright focused ion beam sources based on laser-cooled atoms. *Appl. Phys.*
748 *Rev.* **3**, 011302 (2016).
- 749 47. Mravec, J. *et al.* Tracking developmentally regulated post-synthetic processing of
750 homogalacturonan and chitin using reciprocal oligosaccharide probes. *Dev.* **141**, 4841–4850
751 (2014).
- 752 48. Rigort, A. *et al.* Micromachining tools and correlative approaches for cellular cryo-electron
753 tomography. *J. Struct. Biol.* **172**, 169–179 (2010).
- 754 49. Mastronarde, D. N. Automated electron microscope tomography using robust prediction of
755 specimen movements. *J. Struct. Biol.* **152**, 36–51 (2005).
- 756 50. Kremer, J. R., Mastronarde, D. N. & McIntosh, J. R. Computer visualization of three-dimensional

- 757 image data using IMOD. *J. Struct. Biol.* **116**, 71–6 (1996).
- 758 51. Castaño-Díez, D., Kudryashev, M., Arheit, M. & Stahlberg, H. Dynamo: A flexible, user-friendly
759 development tool for subtomogram averaging of cryo-EM data in high-performance computing
760 environments. *J. Struct. Biol.* **178**, 139–151 (2012).
- 761 52. Castaño-Díez, D., Kudryashev, M. & Stahlberg, H. Dynamo Catalogue: Geometrical tools and data
762 management for particle picking in subtomogram averaging of cryo-electron tomograms. *J.*
763 *Struct. Biol.* **197**, 135–144 (2017).
- 764 53. Zivanov, J. *et al.* New tools for automated high-resolution cryo-EM structure determination in
765 RELION-3. *Elife* **7**, (2018).
- 766 54. Ortega, D. R. *et al.* Repurposing a chemosensory macromolecular machine. *Nat. Commun.* **11**, 1–
767 13 (2020).
- 768 55. Dimchev, G., Amiri, B., Fäßler, F., Falcke, M. & Schur, F. K. Computational toolbox for
769 ultrastructural quantitative analysis of filament networks in cryo-ET data. *bioRxiv*
770 2021.05.25.445599 (2021).
- 771
- 772